Tardi-magmatic iddingsite in the Martian Nakhlite NWA 817

Valentine Megevand, J-C Viennet, C Le Guillou, F Guyot, S Bernard

Geochimica et Cosmochimica Acta xxx (xxxx) xxx

Contents lists available at ScienceDirect

Geochimica et Cosmochimica Acta

journal homepage: www.elsevier.com/locate/gca

Tardi-magmatic iddingsite in the Martian Nakhlite NWA 817

V. Megevand [a,*], J.-C. Viennet [a], C. Le Guillou [b], F. Guyot [a], S. Bernard [a]

[a] Muséum National d'Histoire Naturelle, Sorbonne Université, CNRS UMR 7590, Institut de Minéralogie, Physique des Matériaux et Cosmochimie, Paris, France
[b] Université Lille, CNRS, INRA, ENSCL, UMR 8207 – UMET – Unité Matériaux et Transformations, 59000 Lille, France

ARTICLE INFO

Associate editor: Tomohiro Usui

Keywords:
Iddingsite
Fe/Mg-smectites
Deuteric alteration
Nakhlite
NWA 817
Mars

ABSTRACT

The mineral assemblage referred to as "iddingsite" has been described in Martian meteorites. In Nakhlites, this assemblage is mainly composed of Fe/Mg-rich phyllosilicates (such as serpentine and smectites) associated in some cases with Fe-oxides (such as ferrihydrite, goethite or (titano)magnetite) and carbonates, and occurs either as patches and veinlets in the mesostasis or as veins infiltrating olivines and clinopyroxenes. So far, iddingsite has usually been interpreted as a product of low-temperature (<150 °C) alteration of pre-existing silicates by (sub) surface water. Here, we report results of the petrographic study of a section of NWA 817 revealing that the olivine-hosted iddingsite veins are symmetrically structured with an internal part exhibiting a mica-celadonite composition and an external part displaying a nontronite-saponite composition. These features are consistent with a progressive differentiation of a residual magmatic fluid having infiltrated decompression-induced cracks of olivines at the end of the cooling sequence. We propose that this residual liquid directly produced the ferric mica-celadonite phyllosilicates while triggering the deuteric alteration of the hosting olivine (i.e. oxidative alteration during magma cooling), thereby producing an alteration front made of Fe-nontronite-saponite at the contact with olivine. Altogether, without excluding the possibility that other Nakhlites (such as Lafayette) may have experienced secondary alteration by (sub)surface Martian water, the observations reported in the present study rather point to the tardi-magmatic production of iddingsite in NWA 817.

1. Introduction

Missions to Mars designed to "Follow the Water" and "Explore Habitability" have revealed that early Mars had liquid water running and flooding (at least episodically) on its surface, as evidenced by valley networks, outflow channels, alluvial fans and fluvio-lacustrine sediments (Carr, 1996; Squyres et al., 2004; Grotzinger et al., 2014; Kite and Conway, 2024). Consistently with the past presence of liquid water on Mars, a number of hydrous minerals, such as hydrated salts or clays have been detected from orbit, (e.g., Carter et al., 2013; Sun and Milliken, 2015), on the ground (Bristow et al., 2018; Rampe et al., 2020; Simon et al., 2023), as well as in some of the SNC Martian meteorites (Shergottites-Nakhlites-Chassignites) (e.g., Treiman et al., 2000; Treiman, 2005; Udry et al., 2020). Among SNC, Nakhlites are augite cumulates containing olivine and exhibiting relatively low abundances of interstitial material, the so-called "mesostasis". All Nakhlites are likely derived from the same Martian magmatic edifice that formed ~ 1340 ± 40 Myr ago and were ejected from Mars 11 Myr ago (Bunch and Reid, 1975; Nyquist et al., 2001; Udry and Day, 2018). Variations in the modal abundances of mesostasis and minor minerals, as well as cooling or equilibration rates have been tentatively explained by the extrusion of successive lava flows and/or the relative positions within the "Nakhlite pile-up" (Balta et al., 2017; Jambon et al., 2016; Udry and Day, 2018).

In Nakhlites, iddingsite (a mineral assemblage comprising Fe/Mg-rich clays) occurs either as veins infiltrating olivines and pyroxenes or as patches in the mesostasis. Iddingsite-like assemblages have been previously described in Nakhla (Gooding et al., 1991; Changela and Bridges, 2010; Lee and Chatzitheodoridis, 2016), Governador Valadares (Changela and Bridges, 2010), Lafayette (Treiman et al., 1993; Borg and Drake, 2005; Changela and Bridges, 2010; Tomkinson et al., 2013; Hicks et al., 2014; Lee et al., 2015; Piercy et al., 2022; Tremblay et al., 2024), CeC 022 (Krämer et al., 2020; Krämer Ruggiu et al., 2024), Yamato Nakhlites (Noguchi et al., 2009; Changela and Bridges, 2010), Miller Range Nakhlites (Hallis and Taylor, 2011), and NWA 817 (Gillet et al., 2002; Hicks et al., 2014; Krämer Ruggiu et al., 2024; Lee et al., 2018). The association of iddingsite with oxides (ferrihydrite, goethite or (titano)magnetite), carbonates (siderite), or sulfates (jarosite or gypsum) in some Nakhlites (Lafayette in particular), has led most authors to

* Corresponding author.
E-mail address: valentine.megevand@mnhn.fr (V. Megevand).

https://doi.org/10.1016/j.gca.2025.01.028
Received 7 May 2024; Accepted 17 January 2025
Available online 20 January 2025

interpret iddingsite as a product of the late, secondary alteration of primary silicates by CO_2-rich fluids at relatively low temperatures (e.g. Bridges and Schwenzer, 2012; Tomkinson et al., 2013).

Iddingsite veins in Nakhlites are thus seen as products of aqueous alteration episodes having occurred on Mars (e.g. Bridges and Schwenzer, 2012), at some time between 630 and 740 Myr ago according to the datation of the carbonate-rich iddingsite veins in Lafayette and Y-000593 (Borg and Drake, 2005; Tremblay et al., 2024). Yet, this is in stark contrast with most historical reports: early studies of terrestrial olivine-rich rocks have shown that iddingsite should be interpreted as the product of the oxidative deuteric alteration of olivine rather than as the product of secondary aqueous alteration (Ross and Shannon, 1925; Edwards, 1938; Baker and Haggerty, 1967; Haggerty and Baker, 1967; Eggleton, 1984). Deuteric alteration refers to the alteration of pre-existing minerals in a magma by the residual, differentiated magmatic liquid enriched in water. In contrast to hydrothermal/weathering alteration processes occurring at rather low temperature, deuteric alteration can start at relatively high temperature and pressure, during magma cooling, when the residual, oxidized magmatic fluid (enriched in water and gases) interacts with previously formed minerals.

Both deuteric and late (low T) alteration involve interactions with a water/volatile-rich fluid and lead to the formation of similar complex interstratified phyllosilicates. In other words, olivine iddingsitization can occur over a wide range of temperature conditions, producing secondary phases difficult to differentiate from one another (Sun, 1957; Baker and Haggerty, 1967; Haggerty and Baker, 1967; Goff, 1996; Clément et al., 2007; Hayman et al., 2008; Mitchell et al., 2009). Discriminating between deuteric and late (low T) alteration is thus challenging, but not impossible, as illustrated by a recent study relying on mineralogical investigations conducted at the submicrometer scale on Precambrian monzogabbros of the Kansas basement (Combaudon et al., 2024), which managed to identify iddingsite veins intersecting olivines as products of deuteric alteration rather than as products of late alteration.

Could iddingsite be produced on Mars via oxidative deuteric alteration, i.e. during magma cooling? Recent studies have demonstrated that some Fe/Mg-rich clay minerals in Nakhlites (Nakhla and NWA 5790) are not the products of the aqueous alteration of pre-existing silicates by (sub)surface water but rather tardi-magmatic minerals (Viennet et al., 2020, 2021), as anticipated earlier (Meunier et al., 2012; Berger et al., 2014). Consistently, tardi-magmatic (deuteric) alteration has been proposed to explain the occurrence of high temperature alteration phases in olivine and pyroxene-hosted melt inclusions in MIL 03346 and Nakhla (McCubbin et al., 2009; Filiberto et al., 2014a). Plus, Kuebler (2013) and Kizovski et al. (2020) interpreted iddingsite veins intersecting olivines in shergottites (ALH 77,005 and NWA 7042) as products of deuteric alteration having occurred during magma cooling, before the total solidification of the rock. Thus, tardi-magmatic iddingsite may be more distributed on Mars than anticipated so far, even though no occurrence of it in Nakhlites has yet been reported.

NWA 817 contains more iddingsite than any other Nakhlite (Lee et al., 2018), but no Martian carbonates (Gillet et al., 2002; Hicks et al., 2014). Plus, the iddingsite of NWA 817 exhibits δD values lower than those of the iddingsite of other Nakhlites (Gillet et al., 2002; Krämer Ruggiu et al., 2024; Lee et al., 2018). Although there is no consensus regarding the relative positions of Nakhlites, all authors agree that NWA 817 was produced in a separate lava flow (possibly together with NWA 998) (Balta et al., 2017; Jambon et al., 2016; Udry and Day, 2018). Thus, NWA 817 may not have (or has likely not) experienced the same history as other Nakhlites (including Lafayette) since its production. NWA 817 underwent only moderate shock damages: the only shock-induced features described so far in NWA 817 are mechanical twinning in clinopyroxenes and the micro-fractures in sulfides (Sautter et al., 2002; Chevrier et al., 2011). NWA 817 contains euhedral subcalcic augites (70 vol%), a rather high modal proportion of mesostasis (20 vol% – mainly composed of albitic plagioclase, Si-rich glass and skeletal titanomagnetite) and a rather low number (10 vol%) of zoned Fe-rich olivines (with a Fe/Mg-rich core and a Fe-rich rim) (Sautter et al., 2002; Udry and Day, 2018). Of importance here, the reddish veins of iddingsite-like material intersecting the olivines in NWA 817 have been interpreted so far as products of low temperature aqueous alteration (Gillet et al., 2002; Krämer Ruggiu et al., 2024; Lee et al., 2018). Here we revisit these previous interpretations based on the fine scale mineralogical study of these iddingsite veins, documenting their nature and textural relationships with olivine using scanning and transmission electron microscopies (SEM and TEM) and scanning transmission X-ray microscopy (STXM).

2. Methods

2.1. Scanning electron microscopy

Scanning electron microscopy was performed on a carbon-coated thin section of NWA 817 for imaging with backscattered electrons and energy dispersive X-ray spectroscopy (EDXS) mapping. A probe current of 150 pA at 15 kV was used for EDXS mapping. Two different SEM were used: a SEM-FEG Ultra 55 Zeiss (IMPMC, Paris, France) and a SEM-FEG TESCAN CLARA (PtME MNHN). Hyperspectral EDXS data were processed using the Hyperspy Python-based package (de la Peña et al., 2017). After some binning when necessary, the signal was denoised using PCA and fitted by a series of Gaussian functions. The resulting processed signal was used to produce mineralogical maps.

2.2. Focused ion beam preparations

Four focused ion beam (FIB) ultrathin sections were extracted from the NWA 817 section investigated (Fig. 1) using a FEI Strata DB 235 (IEMN, Lille, France) at low Ga-ion current to minimize mixing of components, creation of vacancies or amorphous layers, local compositional changes, or redeposition of the sputtered material on the sample surface (Bernard et al., 2009; Schiffbauer and Xiao, 2009; Wirth, 2009).

2.3. Scanning transmission X-ray microscopy

Scanning transmission X-ray microscopy (STXM) and X-ray absorption near edge structure (XANES) data were collected using the HERMES STXM beamline at the synchrotron SOLEIL (Belkhou et al., 2015; Swaraj et al., 2017). XANES data were extracted from image stacks collected at energy increments of 0.1 eV scanning energies near the iron $L_{2,3}$ absorption edge (690–740 eV) with a dwell time of 1 ms per pixel to prevent irradiation damage (Wang et al., 2009). Spectral processing was done using the Hyperspy Python-based package (de la Peña et al., 2017). Spectra were corrected using a linear background fitting the region 690–702 keV and normalized with respect to the 715–719 keV region, corresponding to the total Fe quantity probed. Spectra were compared to reference spectra available in Bourdelle et al. (2013) and Le Guillou et al. (2015) to roughly estimate the concentration in Fe^{3+}.

2.4. Transmission electron microscopy

Transmission electron microscopy (TEM) in scanning transmission mode (STEM) was performed on FIB sections using a Thermo Fisher Titan Themis 300 microscope operating at 300 kV (CCM, Lille, France). High resolution images were obtained in STEM mode using the high angle annular dark field detector (HAADF) and a camera length of ~ 115 mm. Hyperspectral EDXS data were collected by a super-X detectors system with four windowless silicon drift detectors, using a probe current of 450 pA with a dwell time of 2 μs per pixel. Hyperspectral EDXS data were processed using the Hyperspy Python-based package (de la Peña et al., 2017). After some binning when necessary, the signal was denoised using PCA and fitted by a series of Gaussian functions.

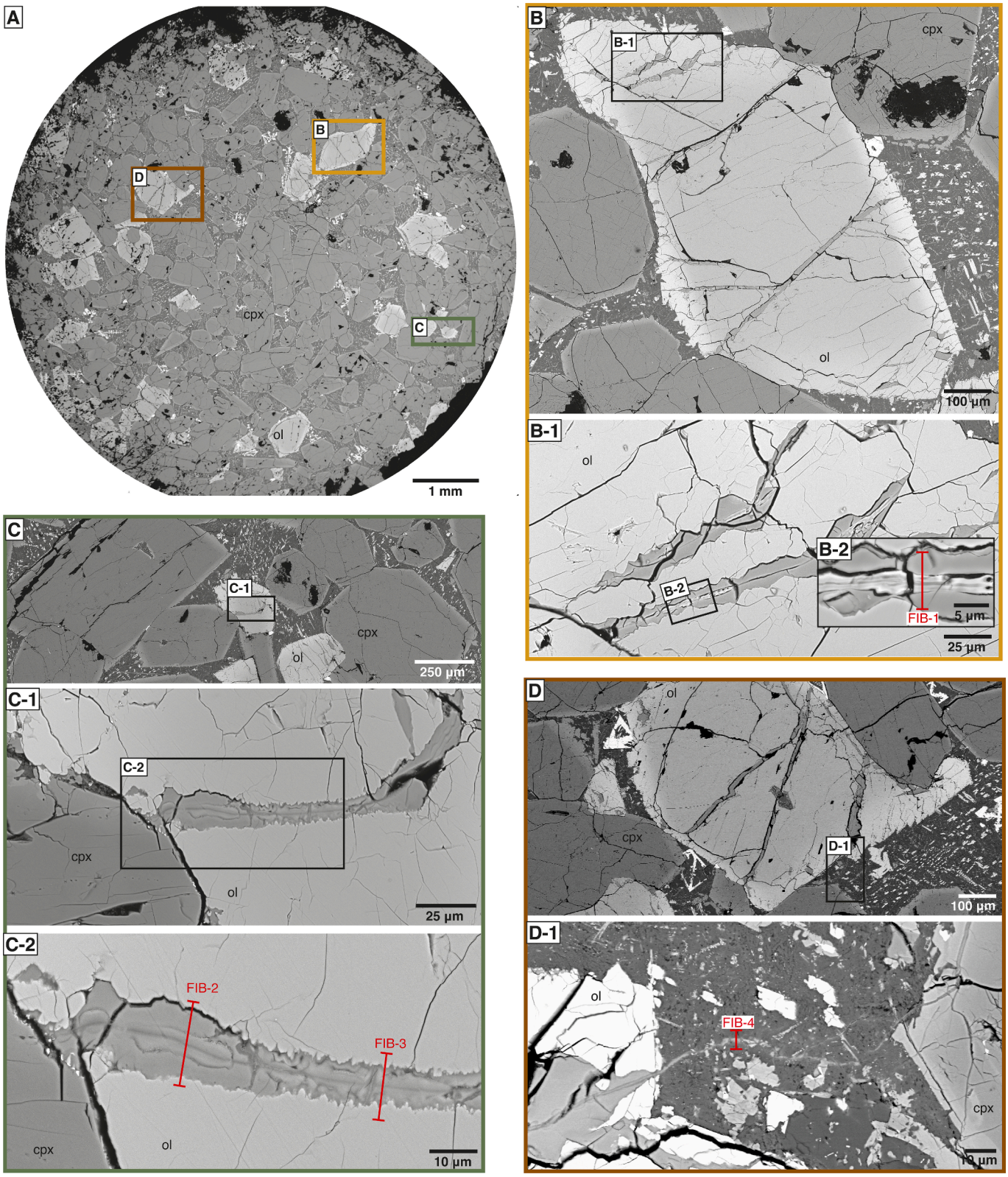

Fig. 1. Back Scattered Electron (BSE) SEM images of the NWA 817 section with the location of the different FIB sections investigated in the present study (continuous red lines). **(A)** General overview of the NWA 817 thin section with the location of the **B** (light brown), **C** (green) and **D** (brown) panels. **ol:** olivine, **cpx:** clinopyroxene.

Spectra quantification was done by integrating the intensities of the Gaussian functions with the Cliff-Lorimer method (Le Guillou and Brearley, 2014). Quantitative composition measurements were obtained using experimentally determined k-factors for major elements and correcting for X-ray absorption within the sample, following the method described by Le Guillou et al. (2024). This revised two-lines approach uses the K and L lines of iron to iteratively calculate the sample's mass thickness and mass absorption coefficient, enabling accurate quantification (in atomic %), even for light elements like C, N, and O. Each pixel was quantified independently, and end-member phases were identified based on major compositional trends. Conventional quasi parallel beam TEM coupled with selected area electron diffraction (SAED) was performed using a JEOL2100 FEG-TEM (IMPMC, Paris, France) operating at 200 kV.

3. Results

3.1. SEM

The section of NWA 817 investigated presents a cumulate texture dominated by primary euhedral augites and olivines embedded in poorly crystalline mesostasis (Fig. 1-*A*). The mesostasis has a general albitic composition and hosts a variety of microphases including augite, skeletal titanomagnetite of about 10–100 µm, chlorapatite and Si-rich phases (Fig. 2). Olivines exhibit a diffuse zoning with a Mg-rich core and a Fe-rich rim which can be as wide as ~ 40 µm (Fig. 2-*B*). These Fe-rich rims exhibit serrated overgrowths at the contact with the mesostasis (Fig. 2-*G to J*). All of the olivines in NWA 817 host 10–30 µm wide veins associated with fractures (Fig. 1-*A and 2*). Most often, veins are perpendicular to the elongation of the olivines (Fig. 1,*2*). EDXS data reveal that these veins are mainly composed of Si, Fe and Mg (Fig. 3, Table 1), and mineralogical maps (Fig. 2-*C,F,J*), show that a part of these veins sometimes extend into the mesostasis (Fig. 2-*F,J*). Patches of a similar material are also observed in the mesostasis, in association with pyroxene (Fig. 2-*F*) or Cl-apatite and Si-rich phases (Fig. 2-*J*). Olivine-hosted veins exhibit chemical contrasts symmetrically distributed from the center to the edges (Fig. 3), with, in most cases, an external part (ev) enriched in Si, an internal part (iv) enriched in Fe, and a central stripe (cs) either less dense or enriched in Mg (Fig. 3-*E*). Textural contact between the external part of the vein and the hosting olivine is mostly characterized by triangular etch pits, which can be associated to small fractures. In some cases, the Fe-rich internal part of the vein is directly in contact with the hosting olivine (Fig. 3-*B and D*) and presents scalloped patterns.

3.2. TEM and STXM-XANES

3.2.1. Olivine-hosted veins

The TEM and STXM-XANES data collected on the FIB-1 section extracted from an olivine-hosted vein confirm its tripartite organization (Fig. 4). The central stripe is rather dark on STEM images, as is the external part of the vein, while the internal part is lighter (Fig. 4-*B*).

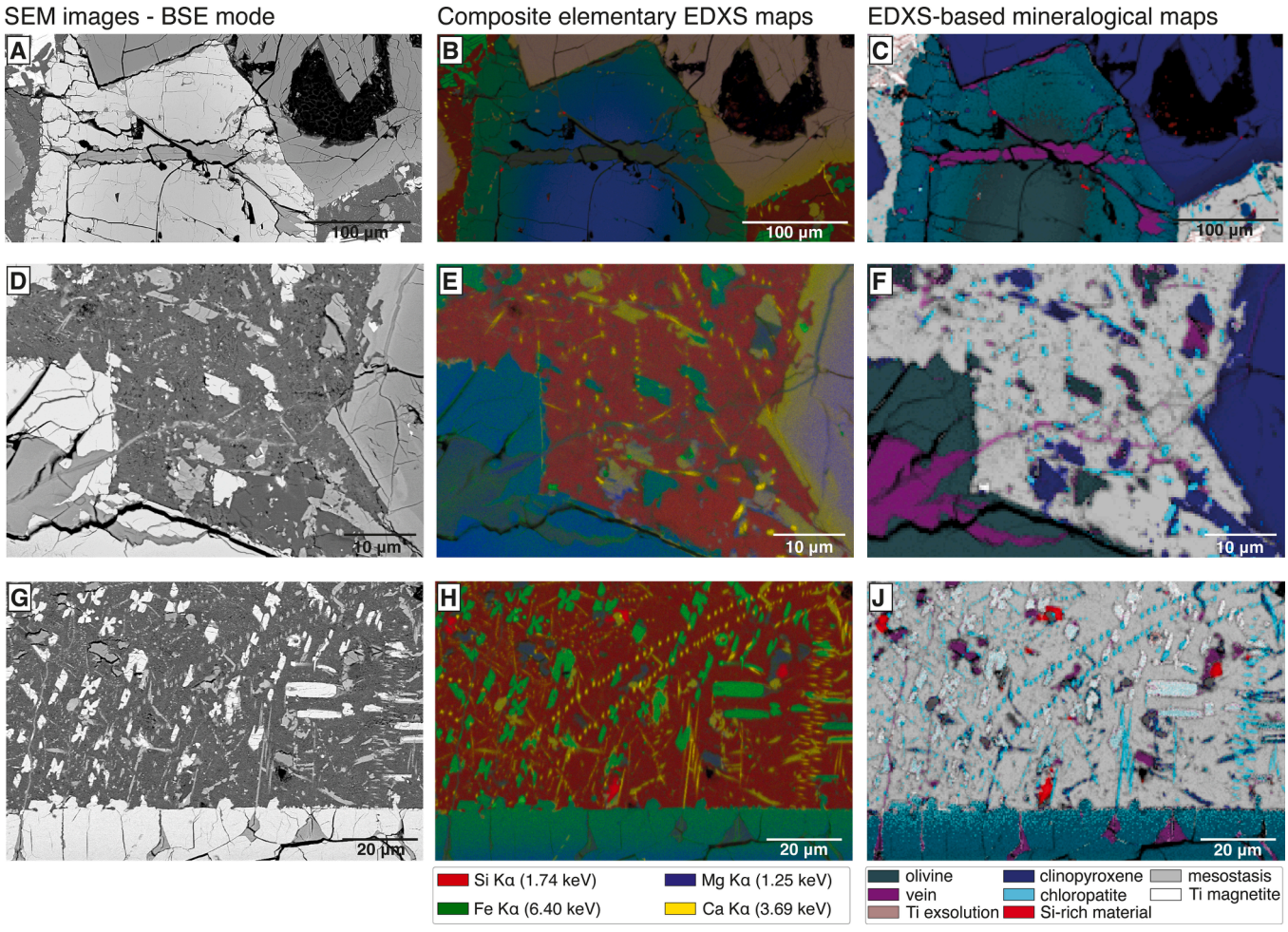

Fig. 2. SEM images showing olivine-hosted veins. **(A), (D)** and **(G)** are SEM images (BSE mode), **(B), (E)** and **(H)** are the corresponding composite color elementary EDXS maps (with Fe in green, Si in red and Mg in blue), and **(C), (F)** and **(J)** are the corresponding EDXS-based mineralogical maps. The vein on images D-E-F prolongates into the mesostasis and the clinopyroxene, while most of the veins on images G-H-J do not.

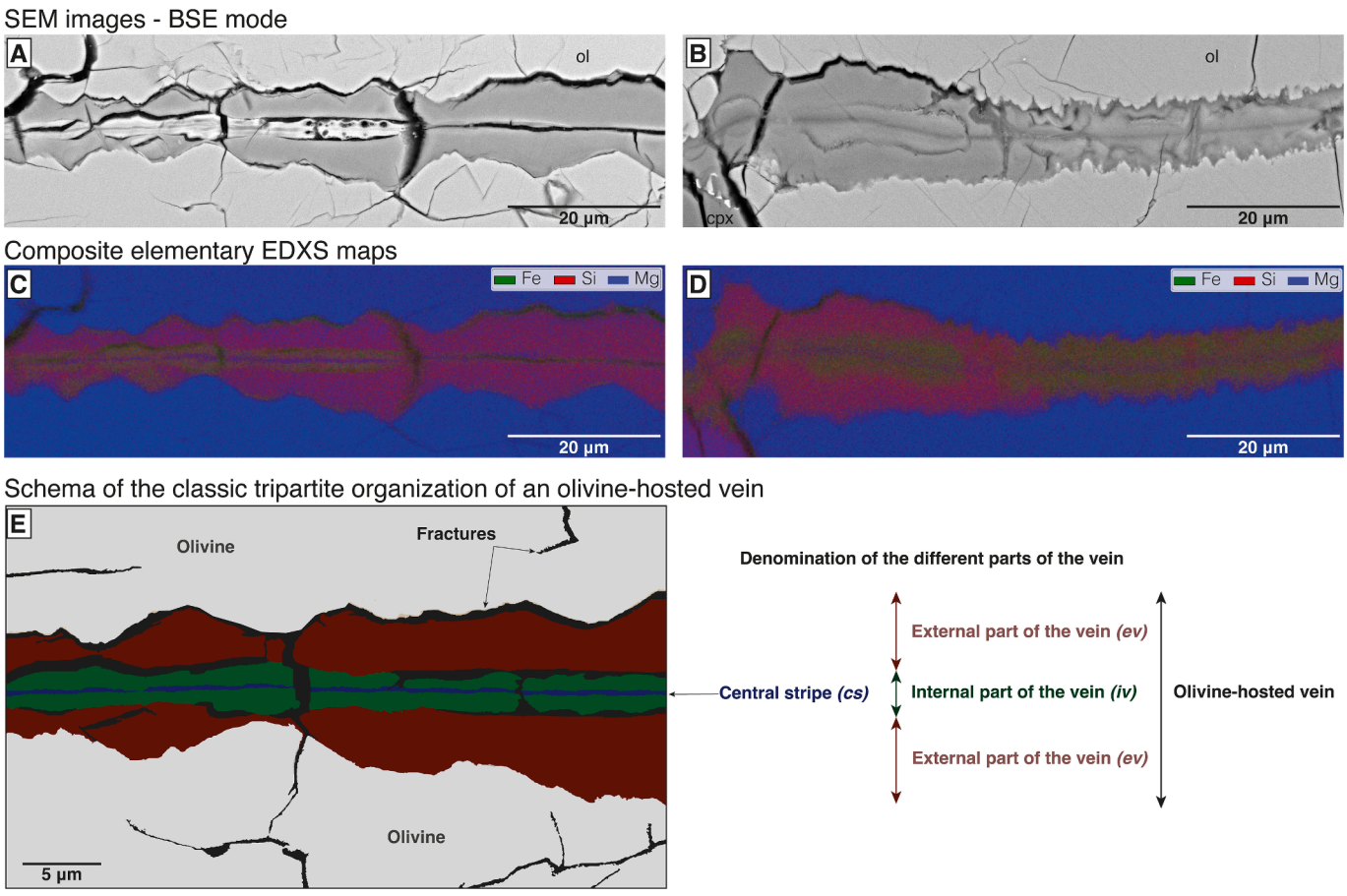

Fig. 3. SEM images, EDXS maps and schematic interpretation of olivine-hosted veins in NWA 817. **(A)** and **(B)** are SEM images (BSE mode) of two veins hosted in different olivines (see Fig. 1-B and 1-C respectively, for the precise location of the veins). **(C)** and **(D)** are the corresponding composite color elementary EDXS maps ((with Fe in green, Si in red and Mg in blue), and the schematics diagram in **(E)** shows the most common tripartite organization of an olivine-hosted vein, with the external part of the vein **(ev)**, the internal part of the vein **(iv)** and the central stripe **(cs)**.

Table 1
Elemental compositions of the different phases identified in atomic percents. Composition was re-calculated on a 100 at.% basis using the mean EDXS spectra of each phase for the major elements Si-Fe-Mg-Al-Ca-Na-K. Olivine composition was calculated using the FIB-3 section. External, internal, and central vein compositions were calculated using the FIB-1 section. Composition of phases from the mesostasis were calculated using FIB-4 section.

Elementary composition in atomic %														
	Si	2σ	Fe	2σ	Mg	2σ	Al	2σ	Ca	2σ	Na	2σ	K	2σ
Vein within the olivine														
Olivine	33.6	0.4	37.3	0.4	26.0	0.4	1.1	0.1	0.9	0.1	1.0	0.1	0.2	0.0
External part	47.2	0.6	39.6	0.5	7.5	0.3	1.4	0.1	0.4	0.1	1.7	0.1	2.3	0.1
Internal part	35.2	0.5	51.6	0.5	2.7	0.2	4.0	0.2	3.6	0.1	1.6	0.1	1.2	0.1
Central stripe	45.3	0.6	35.5	0.4	12.3	0.3	2.4	0.1	2.2	0.1	1.4	0.1	1.0	0.1
Veinlet within the mesostasis														
Mesostasis	66.6	0.3	0.6	0.0	0.4	0.0	25.2	0.2	2.1	0.1	3.3	0.1	1.8	0.1
Homogeneous area	47.5	0.3	27.2	0.2	10.0	0.2	7.0	0.1	1.6	0.1	4.3	0.1	2.4	0.1
Porous area	44.9	0.3	22.6	0.2	4.4	0.1	10.3	0.1	2.2	0.1	11.9	0.2	3.8	0.1
Layered material	47.4	0.3	19.6	0.2	4.5	0.1	14.2	0.2	1.4	0.0	5.7	0.1	7.1	0.1

Confirming SEM-EDXS data, TEM-EDXS data show that the central stripe contains more Mg and less Fe than the internal part, while the external part contains more Si *(Fig. 4-D)*. At this level of magnification, an Fe-rich zone is observed at the center of the central stripe (white arrow in Fig. 4-*D*). XANES data reveal a high level of oxidation, with a even higher concentration in Fe^{3+} in the central stripe and the internal part of the vein (with spectra similar to the 100 % Fe^{3+} reference from Bourdelle et al., 2013 – Fig. 4-*E*).

TEM images, Fast Fourier Transform (FFT) and SAED patterns indicate that the different parts of the vein consist of nanocrystalline material *(Fig. 4-C)*. The central stripe contains 20–30 nm long layered material with 9.5 Å d-spacings which do not exhibit any preferential orientation *(Fig. 4-C)*. Although crystals are difficult to distinguish on bright field images of the internal and external parts of the veins *(Fig. 4-C)*, both SAED patterns display at least two rings, consistent with d-spacings of approximately 1.5 and 2.6 Å, demonstrating that the material is mainly made of phyllosilicates (Meunier, 2005; Meunier et al., 2008). Precisely, the SAED patterns of the external part of the vein exhibits a 06.33 reflection at 1.55 Å and an additional 0.211 reflection at 4.52, which is consistent with nontronite (Baron et al. 2016; Fox et al. 2021). Additionally, HRTEM images and FFT patterns of bright-field images reveal interplanar d-spacings of about 10 Å *(Fig. 4-C)*,

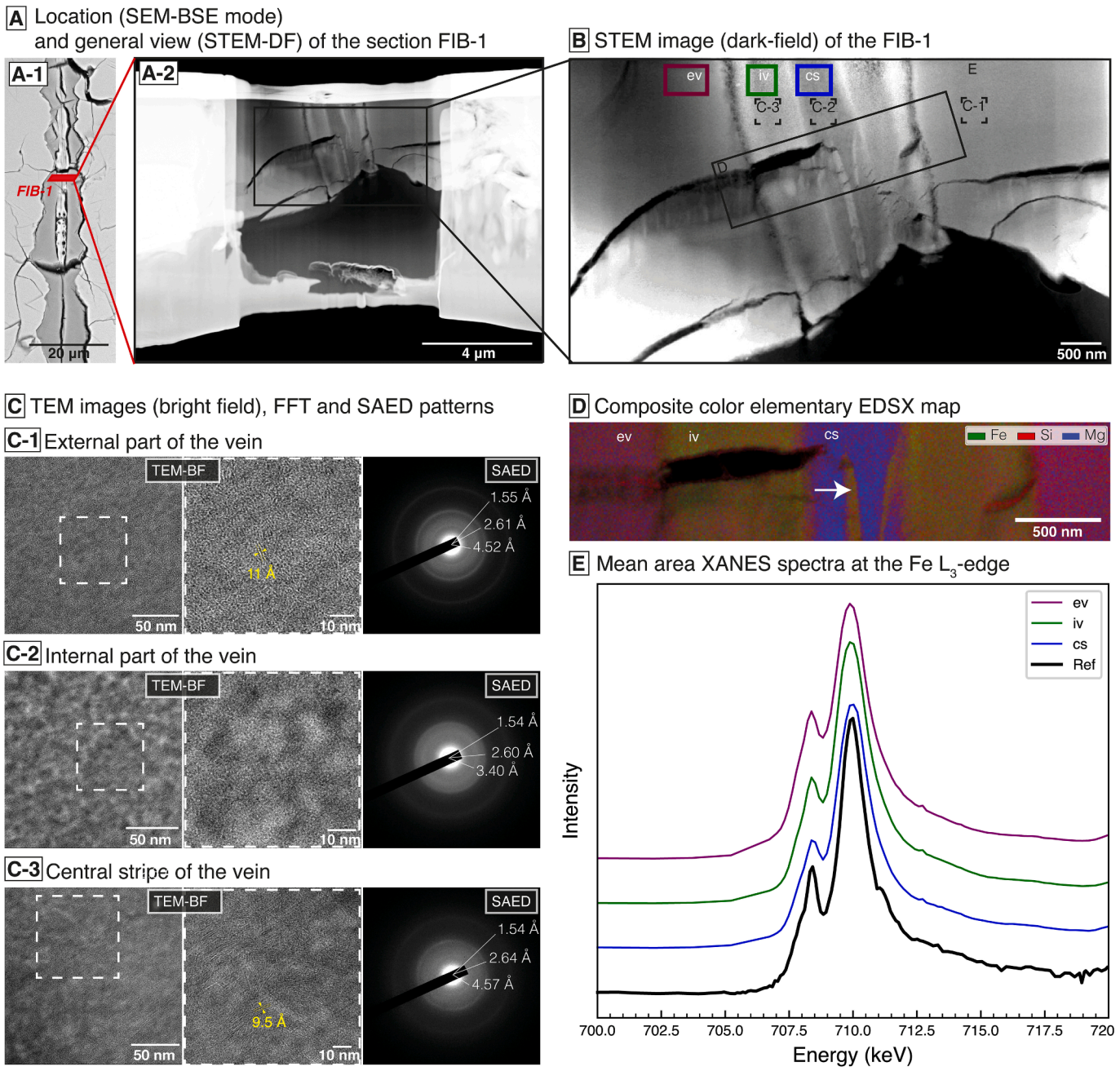

Fig. 4. TEM and STXM data collected on the FIB-1 section, intersecting an olivine-hosted vein. (A) Location and general view of FIB-1 in STEM (Dark Field, DF, mode). (B) STEM-DF image of the olivine hosted vein exhibiting the classic tripartite organization with the external part of the vein (ev), the internal part of the vein (iv) and the central stripe (cs). Dashed squares indicate the location of TEM images shown in (C). Plain black square indicates the location of (D). (C) Amplitude contrast images in bright field and associated SAED. (D) Composite color elementary EDXS maps with Fe (green), Si (red) and Mg (blue). The external part appears Si-enriched, the internal part Fe-enriched and the central stripe Mg-enriched. The white arrow indicates an additional feature within the central stripe with a composition similar to the internal part of the vein. (E) Mean XANES spectra of the different areas of the olivine-hosted vein highlighted in (B) compared to the to the 100 % Fe^{3+} reference from Bourdelle et al. (2013).

consistent with either micas or smectites (Hicks et al., 2014; Evans et al., 2017).

EDXS data informed about the composition of the different parts of the vein (Table 1), even though identifying phyllosilicates solely based on unit formula is challenging given the existence of various solid solutions and the possible interstratification (Grauby et al., 1994). A solution is to use a $M^{\pm}$-4Si-$3R^{2+}$ ternary diagram (Fig. 5), allowing separating solid-solution domains of both di- and trioctahedral species, as well as mixtures and mixed-layered minerals (Meunier and Velde, 1989; Meunier et al., 2013). The $M^{\pm}$ pole represents the total electrical charge provided by interlayer cations ($Na + K + 2Ca$), the 4Si pole represents the tetrahedral charge ($Si/4$), and the 3R pole represents the number of bivalent ions integrated in the octahedral sheets with $3R = (Mg^{2+} + Fe^{2+} + Mn^{2+})/3$. Note that the content in Fe^{2+} has been considered as being close to zero given the resemblance between the XANES spectra of these phyllosilicates with that of the 100 % Fe^{3+} reference from Bourdelle et al. (2013) (Fig. 4-E). On such a ternary diagram, the olivine-hosted vein defines three distinct pools. The $4Si/3R^{2+}$ values are constant for both the internal and external part of the vein, but the three different parts of the vein exhibit distinct $M^{\pm}$ values

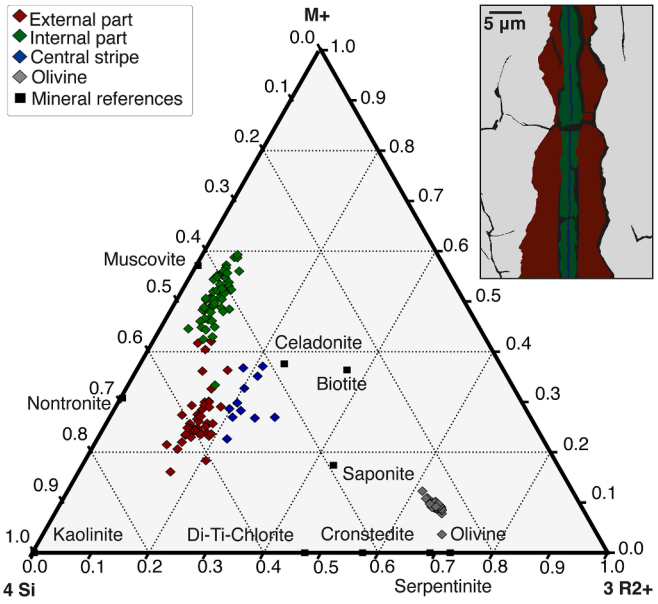

Fig. 5. Triplot ($M^{\pm}$-4Si-$3R^{2+}$ ternary plot) showing the chemical compositions of the different parts of the olivine-hosted veins estimated from EDXS data. The $M^{\pm}$ pole represents the total electrical charge provided by interlayer cations (Na + K + 2Ca), the 4Si pole represents the tetrahedral charge (Si/4), and the 3R pole represents the number of bivalent ions integrated in the octahedral sheets with $3R = (Mg^{2+} + Fe^{2+} + Mn^{2+})/3$. Note that the content in Fe^{2+} has been considered as being close to zero given the resemblance between the XANES spectra of these phyllosilicates with that of the 100 % Fe^{3+} reference from Bourdelle et al. (2013). The schematics diagram on the right shows the most common tripartite organization of an olivine-hosted vein, with the external part of the vein, the internal part of the vein and the central stripe with the same color code.

indicating a different permanent charge. The internal part of the vein has the highest permanent charge, with a composition lying between muscovite, biotite and celadonite end-members, in contrast to the external part of the vein which has the lowest permanent charge and falls between the nontronite-saponite end-members. The central stripe has the highest magnesium content (12.5 ± 0.5 at.% – Table 1) and falls between the celadonite-saponite-nontronite end-members.

3.2.2. Focus on phyllosilicates and olivine contacts

The FIB-2 and FIB-3 sections were extracted from the same olivine-hosted vein (Fig. 6-*A and* Fig. 7-*A)*. Nevertheless, in contrast to the classical tripartite structure (central stripe – internal part – external part) of other veins, the vein does not exhibit an external part in the FIB-3 area: the central stripe is only surrounded by an internal part directly in contact with the hosting olivine. TEM and STXM-XANES investigations confirmed the presence of the phyllosilicates identified in the FIB-1 section, i.e. the celadonite central stripe, the mica-celadonite mixture of the internal part of the vein, and the nontronite-saponite mixture in the external part of the vein (the latter being only present in FIB-2).

As observed on the FIB-2 section, the transition between the nontronite-saponite of the external part of the vein and the olivine is characterized by a 100–200 nm thick, porous area exhibiting nano-voids visible in both STEM-Dark field mode *(*Fig. 6-*B)* and TEM-Bright field mode *(*Fig. 6-*C)*. In STEM, lighter dots are also observed and correlated with a local iron enrichment *(*Fig. 6-*C-D)*. SAED patterns (Fig. 6-*C*) display at least two rings, consistent with d-spacings of approximately 1.55 and 2.63 Å, also demonstrating that the material is mainly made of phyllosilicates (Meunier, 2005; Meunier et al., 2008). HRTEM images and FFT patterns of bright-field images reveal interplanar d-spacings of about 10 Å *(*Fig. 6-*C)*, consistent with either micas or smectites (Hicks et al., 2014; Evans et al., 2017). As observed on the FIB-3 section, the contact between the internal part of the vein and the olivine is different. Bright-field TEM imaging *(*Fig. 7-*C)* shows a transitional zone composed of two intermixed layers – a porous zone (~100 nm thick) directly contacting the olivine and an inner 100 nm-thick layer comprising palisade-shaped crystallites measuring up to 50 nm and oriented towards the inner part of the vein. The ring d-spacings of 10.1 and 13.1 Å observed in HRTEM images *(*Fig. 7-*C)* and the d-spacings of ~ 1.52, 2.60 and 3.47 Å estimated from SAED patterns *(*Fig. 7-*C)* confirm the phyllosilicate nature of this layer, possibly composed of interstratified micas/smectites or chlorites/smectites. As in FIB-2, a slight Fe enrichment is observed at the contact with olivine *(*Fig. 7-*D)*.

3.2.3. Veinlets within the mesostasis

The FIB-4 section was extracted from the mesostasis across a veinlet in the continuation of an olivine-hosted vein *(*Fig. 8-*A)*. Besides the small NaCl crystals of about 50 to 250 nm which are interpreted as resulting from the beam-induced vaporization and redeposition of plagioclase sodium and chlorine, three distinct materials can be identified. A first material, at the center of the veinlets, exhibits an homogenous texture (Fig. 8-*C*) and a higher concentration of magnesium (10 ± 0.5 at.%) compared to the rest of the veinlet (4.5 ± 0.5 at.% – Fig. 8-*D* and Table 1). Another more porous material is observed at the contact with the mesostasis and within smaller lateral veinlets (Fig. 8-*C*) and appears to be enriched in iron *(*Fig. 8-*D)*. Last, a well-crystallized layered material is present either as masses at the contact with the porous areas or as separate patches *(*Fig. 8-*B)*. This material is made of 100–200 nm-long layers *(*Fig. 8-*C)* with interplanar spacings of about 10.1 Å according to FFT patterns and HRTEM images. All these different material areas display SAED patterns with two diffuse rings consistent with d-spacings of ~ 1.5 to ~ 1.6 Å and ~ 2.6 to ~ 2.7 Å *(*Fig. 8-*C)*, suggesting a phyllosilicate nature. Of note, the SAED pattern of the well-crystallized layered material exhibits additional rings created by multiple diffraction spots at interplanar d-spacings of 1.28, 1.44, 2.18, and 3.07 Å *(*Fig. 8-*C-4)*. This layered material, closely associated with apatite and Ti-magnetite grains, exhibits sharp contact with clinopyroxenes *(*Fig. 9*)*.

The compositions of these different materials were estimated from EDXS data and plotted in a $M^{\pm}$-4Si-$3R^{2+}$ ternary diagram *(*Fig. 10 *&* Table 1*)*. The homogeneous material shows a range in compositions falling between the high-charge mica-celadonite and the nontronite-saponite, overlapping with the internal parts and the central stripes of the veins hosted by olivines although it exhibits slightly higher Al content (7 ± 0.5 at.% *vs* 4 ± 0.5 at.% and 2.5 ± 0.5 at.%). The porous area falls outside the range of the different phyllosilicate solid solutions while the layered material exhibits an intermediate composition between mica and celadonite, but with lower Fe content than the internal part of the olivine-hosted veins.

4. Discussion

4.1. A tardi-magmatic origin of the olivine-hosted veins

The detailed examination of the olivine-hosted veins in NWA 817 has revealed that these veins are structured in three parts composed of nanocrystallized phyllosilicates, ranging from a mica-celadonite composition to a nontronite-saponite composition. Thus, the veins in NWA 817 could be interpreted as tardi-magmatic in origin, i.e. as having precipitated during the alteration of olivine by the residual magmatic fluid having undergone progressive differentiation *(*Fig. 11*)*. During the ascent to the surface of the partially crystallized magma already containing olivines and pyroxenes, the extrusion-induced decompression has likely created cracks in the already crystallized olivines *(*Fig. 11-*A)*. The rapid cooling led to the solidification of the mesostasis, leaving a residual, differentiated magmatic fluid with a micaceous composition which have seeped into the olivine cracks *(*Fig. 11-*B)*, starting to alter the olivine in an oxidative deuteric alteration process and crystallizing into the ferric

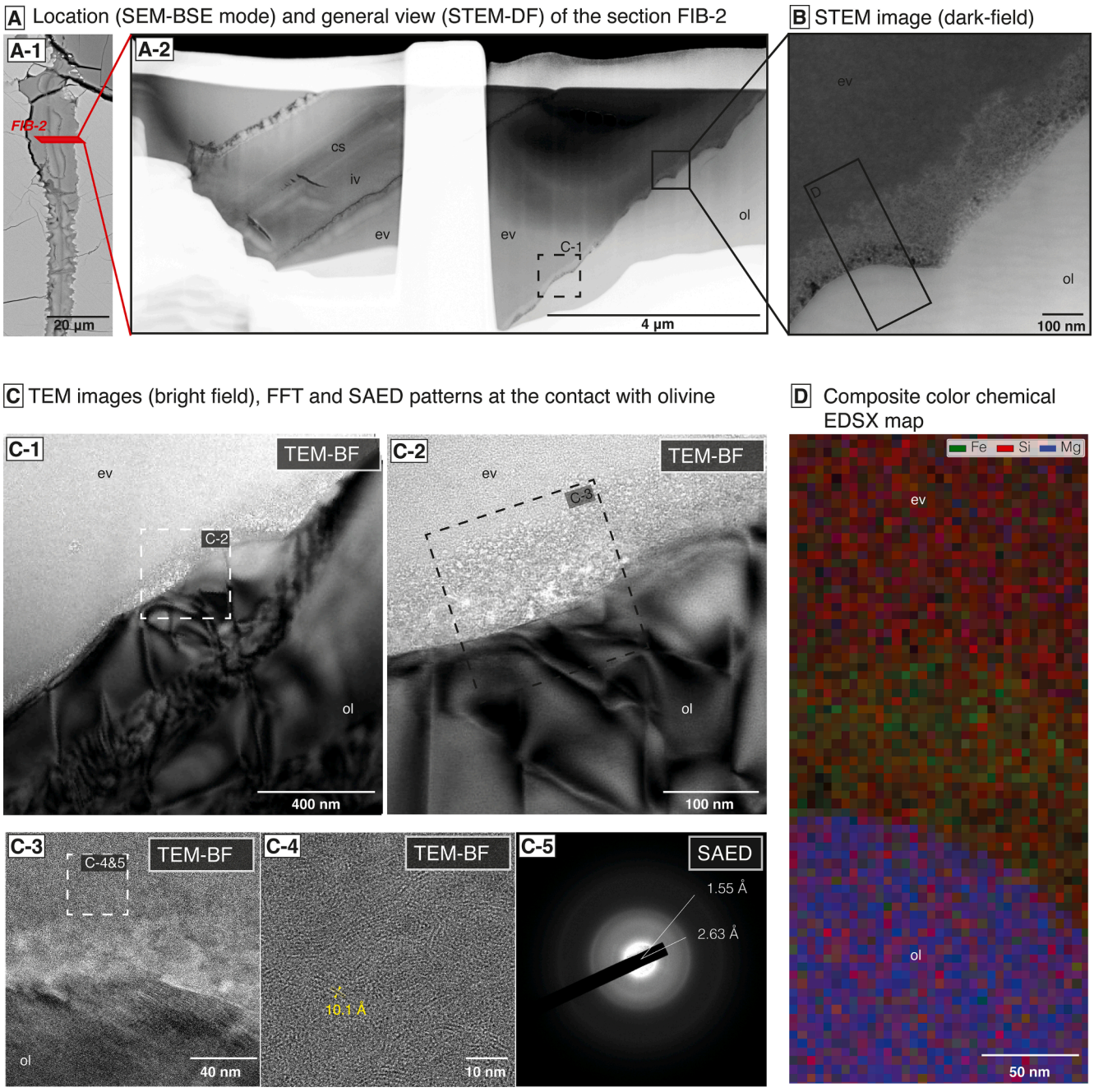

Fig. 6. TEM data collected on the FIB-2 section showing the contact between the external part of the vein and the hosting olivine. **(A)** Location and general view of FIB-2 in STEM (Dark Field, DF, mode). Dashed square indicates the location of the TEM image **C-1**. Plain square indicates the location of the STEM image **(B)**. **(B)** STEM-DF image of the contact with olivine exhibiting a porous transition zone. **(C)** Amplitude contrast images in bright field **(C-1 to C-4)** and associated SAED **(C-5)**. **(D)** Composite color elementary EDXS maps with Fe (green), Si (red) and Mg (blue). The transition zone at the contact with olivine appears enriched in Fe.

mica-celadonite phyllosilicates composing the internal part and the central stripe of the veins *(*Fig. 11*-C)*. Such precipitation has left a last fluid trapped between the olivine and the phyllosilicates composing the internal parts of the veins. This last fluid, enriched in water and in strong disequilibrium with the fayalite, continued to dissolve the hosting olivine, producing Fe-nontronite-saponite enriched in Mg compared to the micas composing the internal part of the vein *(*Fig. 11*-D)*.

This scenario is fully supported by the observations reported here. First, the structure of the veins – with parts sub-parallel to each other and perpendicular to the elongation of the hosting olivines *(see* Fig. 1*-B)* – differs from the reaction-driven "Frankenstein" cracks which form in serpentinization contexts via hydraulic fracturing and which are characterized by a central vein feature lined with a secondary set of orthogonally oriented cracks (Evans et al., 2020), without mentioning the multiple evidence of fluid circulation which are not observed in NWA 817. The veins in NWA 817 rather resemble the sealed cracks commonly observed in olivines from kimberlites having formed due to decompression during magma ascent (Brett et al., 2015). The structure of the veins in NWA 817 thus appears more consistent with fluid infiltration and precipitation within pre-existing fractures or cracks generated by decompression. On top of that, the palisadic fabric of the phyllosilicates at the contact between the internal part of the vein and the olivine *(*Fig. 7*-C-1 to C-3)* – also observed in non-altered subaerial hawaiites (Meunier et al., 2008) – is typical of the precipitation from an oversaturated solution at the wall of diktytaxitic voids (Grigor'ev and Brenner, 1965; Meunier et al., 2008).

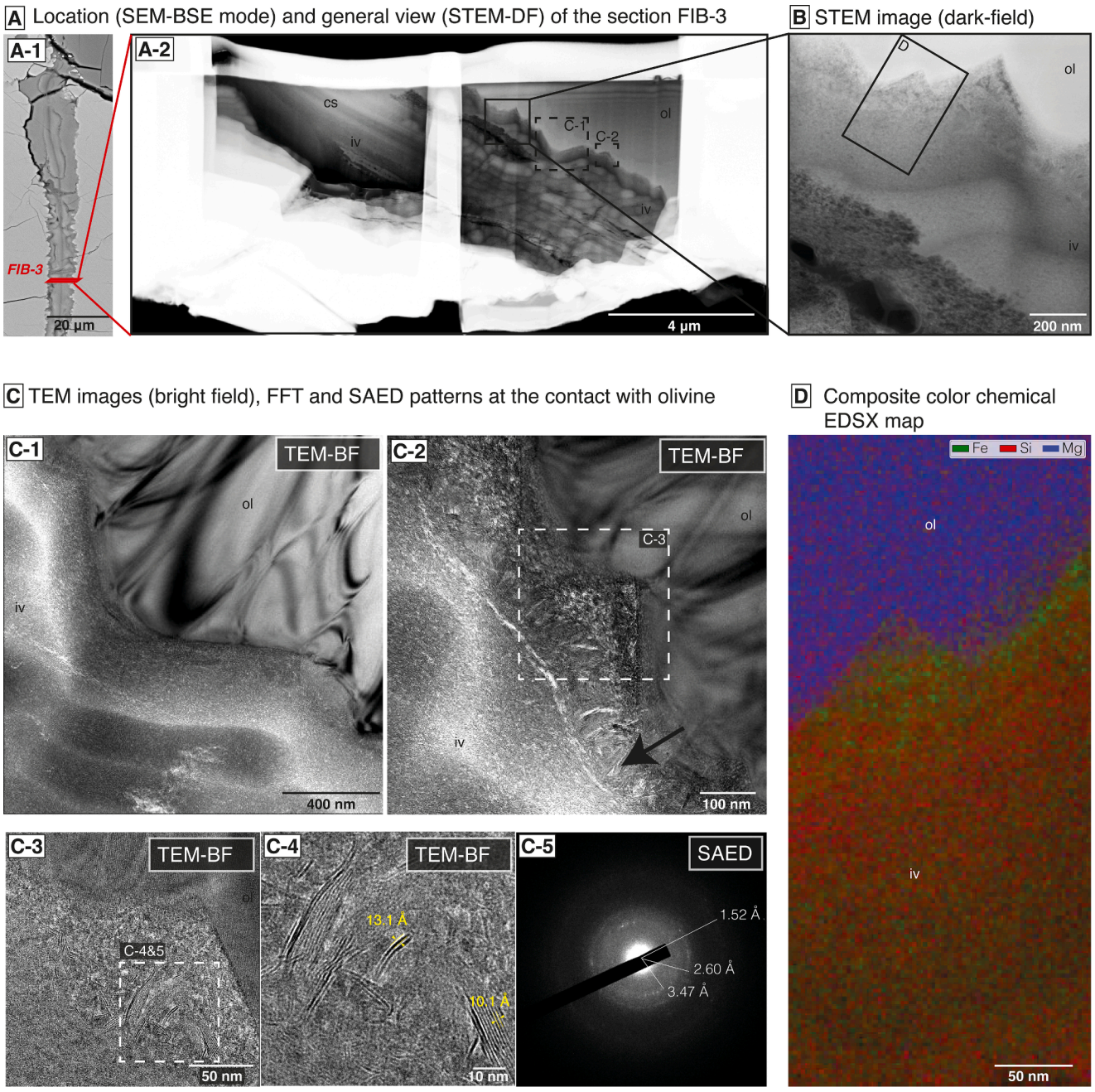

Fig. 7. TEM data collected on the FIB-3 section showing the contact between the internal part of the vein and the hosting olivine. **(A)** Location and general view of FIB-3 in STEM (Dark Field, DF, mode). Dashed square indicates the location of the TEM image **C-1 and C-2**. Plain square indicates the location of the STEM image **(B)**. **(B)** STEM-DF image of the contact with olivine. **(C)** Amplitude contrast images in bright field **(C-1 to C-4)** and associated SAED **(C-5)**. Palisadic lamellar material is observed at the contact with olivine in **C-2 and C-3**. **(D)** Composite color elementary EDXS maps with Fe (green), Si (red) and Mg (blue). The transition zone at the contact with olivine appears slightly enriched in Fe.

The micaceous to celadonite composition of the internal part of the veins strongly argues for a late-magmatic origin, i.e. a crystallization at high temperature from a residual magmatic fluid (600 to 750 °C – Saltas et al., 2020), rather than to a low temperature process, i.e. secondary aqueous alteration. The composition of smectites may also provide insights on their temperature of formation, since dehydroxylation of saponite occurs at ~ 750 °C (Kloprogge and Ponce, 2021) while that of nontronite occurs at ~ 450 °C (Ding and Frost, 2002). However, more accurate temperature estimation would require precise estimates of water content and pressure conditions, which are not constrained here. Of note, a rather rapid cooling of the melt is needed to produce the clay mineral assemblage observed here, as demonstrated experimentally (Nakazawa et al., 1992; Yamada et al., 1994; Yamada, 1995; Tamura et al., 2000; Kalo et al., 2010). For instance, Yamada et al. (1995) demonstrated that the fast cooling of a hydrous silicate melt (1500 °C/min) will produce smectites together with low amounts of coesite, kyanite and jadeite, while the slow cooling of the same melt (150 °C/min) will only produce coesite, kyanite, jadeite and clinoenstatite. These results demonstrated that smectite crystals are formed metastably during the quenching of the high-pressure and high-temperature hydrous silicate melt.

Chemically, the Al enrichment of the internal part of the veins is consistent with a mesostasis-originated fluid while geometrically, the occurrence of internal parts within some central stripes (cf Fig. 4-*D)* is

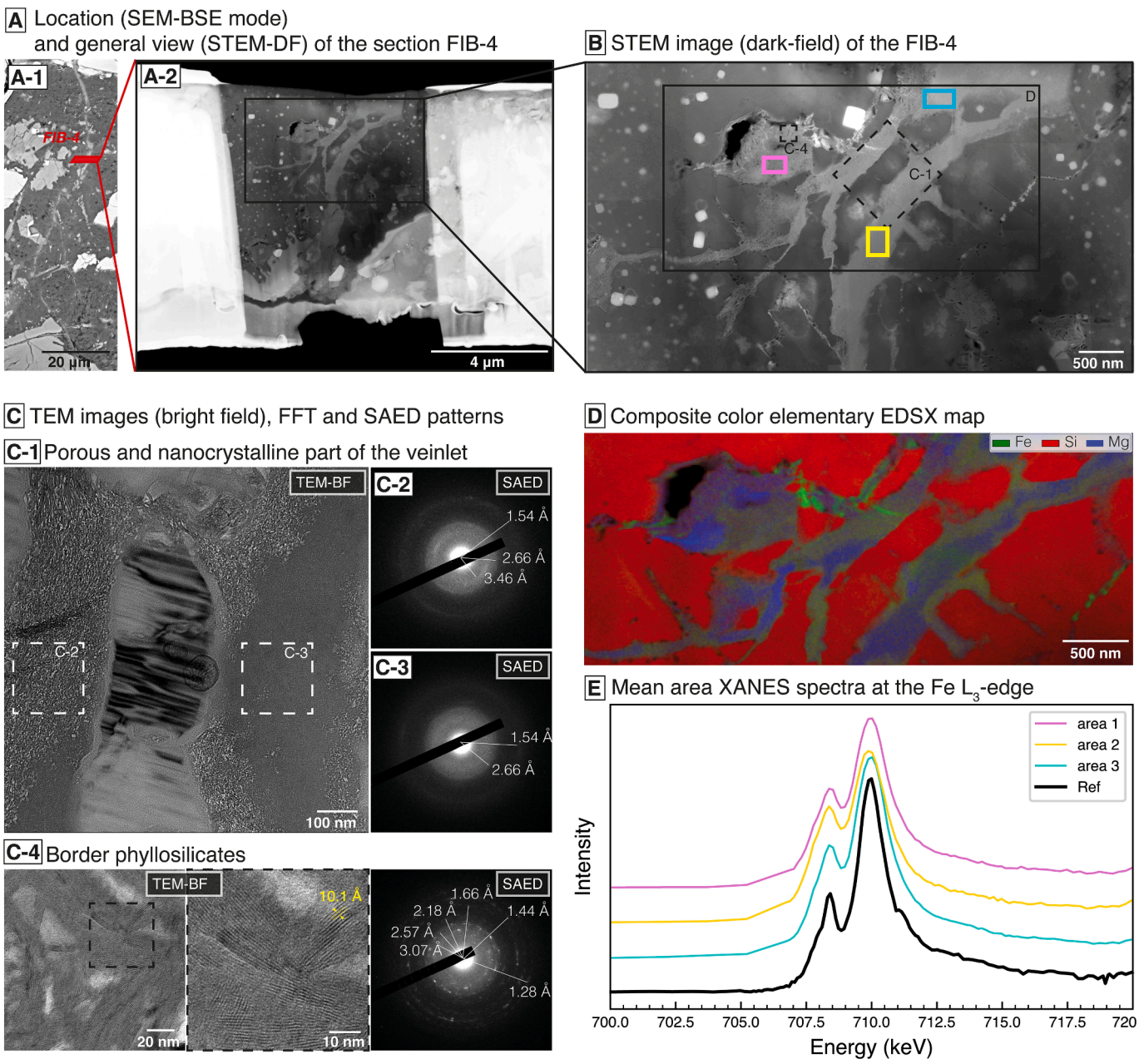

Fig. 8. TEM and STXM data collected on the FIB-4 section intersecting a mesostasis vein prolongating of an olivine-hosted vein. (A) Location and general view of FIB-4 in STEM (Dark Field, DF, mode). (B) STEM-DF image of the olivine hosted vein exhibiting the classic tripartite organization with the external part of the vein (ev), the internal part of the vein (iv) and the central stripe (cs). Dashed squares indicate the location of TEM images shown in (C). Plain black square indicates the location of (D). (C) Amplitude contrast images in bright field and associated SAED. (D) Composite color elementary EDXS maps with Fe (green), Si (red) and Mg (blue). The nano crystallized area appears Mg-enriched while the porous area appears Fe-enriched. (E) Mean XANES spectra of the different areas of the mesostasis vein highlighted in (B) compared to the to the 100 % Fe^{3+} reference from Bourdelle et al. (2013).

consistent with the synchronous crystallization of the internal part and the central stripe. The triangular etch pit geometry of the external part of the veins *(Fig. 3-A)*, and the Fe-enrichment at the olivine contact *(Fig. 6-B and C)*, suggest that the hosting olivine has undergone a dissolution process (Baker and Haggerty, 1967; Haggerty and Baker, 1967; Velbel, 2009). The nontronite-saponite external part of the veins is thus interpreted as the product of the continued oxidative deuteric alteration of the olivine, which likely started at the moment the penetration of the residual magmatic fluid begins, i.e. during the crystallization of the internal part. Consistently, DePasquale and Jenkins (2022) experimentally showed that nontronite can form from a mixture of mafic and felsic minerals (such as fayalite, magnetite, albite and quartz), i.e. that a residual, differentiated magmatic liquid interacting with fayalite can produce smectite such as nontronite. Plus, the mica-celadonite to nontronite-saponite sequence (from the internal to the external parts of the veins defines a decreasing trend in permanent phyllosilicate charges from Ca-rich micas to K-rich smectites, consistent with a magmatic cooling differentiation sequence (Fig. 12 – Meunier et al., 2008). Last, the very high Fe^{3+} content of the external part of the veins is fully consistent with an oxidative alteration of the olivine, while the even higher content in Fe^{3+} of the internal part of the veins *(Fig. 4-E)* is consistent with a residual liquid having been more CO_2-rich during the precipitation of the internal part of the veins and more H_2O-rich during the precipitation of the external part of the veins (Kelley, 1996).

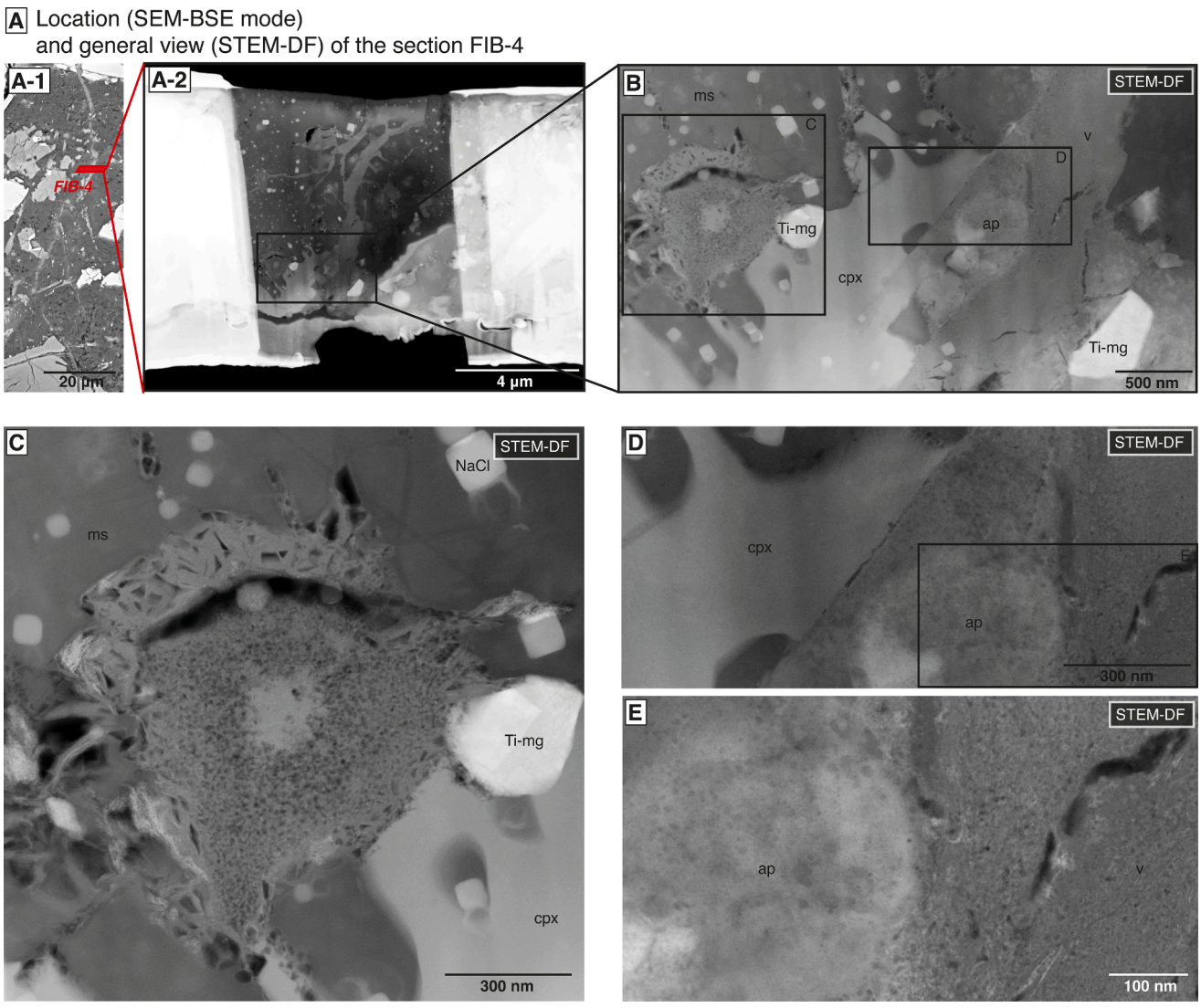

Fig. 9. TEM images of the FIB-4 section. **(A)** Location and general view of FIB-4 in STEM (Dark Field, DF, mode). **(B)** STEM-DF image of the mesostasis vein at the contact with small mesostasis clinopyroxene. Plain squares indicate the location of **(C)** and **(D)**. **(C)** Zoom on a patch of lamellar phyllosilicates arranging around highly porous material, exhibiting a linear contact with the clinopyroxene. **(D)** Zoom on the contact between the vein with clinopyroxene and chlorapatite. **(E)** Zoom showing intermixed chlorapatite with phyllosilicates of the vein. Legend: v vein, cpx clinopyroxene, ap chlorapatite, Ti-mg titano-magnetite, NaCl superficial NaCl crystals.

4.2. Tardi-magmatic phyllosilicates: terrestrial and Martian precedents

A number of studies have previously concluded on the magmatic origin of some phyllosilicates in terrestrial and Martian rocks. Meunier et al. (2008) reported the formation of tardi-magmatic phyllosilicates in the mesostasis of the inner, unaltered section of a basaltic body from the Mururoa Atoll (French Polynesia). The proposed scenario of formation of these phyllosilicates did not include any alteration of pre-existing silicates, but the progressive oversaturation of a residual water-rich magma. Such oversaturation led to the production of a clay matrix embedding euhedral apatite and pyroxene, with clays filling all dikty-taxitic voids (i.e. open spaces in an angular network of phenocrysts), forming a palisadic texture and covering all the unaltered surfaces of biotite or feldspar phenocrysts (Meunier et al., 2008, 2012). The occurrence of such magmatic Fe/Mg clays has also been reported in flood basalts forming the Parana Basin (Brazil) (Schenato et al., 2003) and in quartz-syenite representing the ultimate differentiation products of the magmatic reservoir of the Piton des Neiges stratovolcano (Réunion Island) (Berger et al., 2018). Similar magmatic clay minerals have also been reported in Martian Nakhlites (Viennet et al., 2020, 2021), confirming early anticipations (Meunier et al., 2012; Berger et al., 2014). Veinlets and patches of phyllosilicates, with a smectite-celadonite composition, enveloping pores of 100–300 nm and mingled with a porous substance have been observed both in Nakhla and NWA 5790 (Viennet et al., 2020, 2021). These clay minerals have been interpreted as having directly precipitated from a water-rich fluid exsolved from the Cl-rich parental melt of the Nakhlites during igneous differentiation (Viennet et al., 2020, 2021), Nakhlites having likely evolved, as Chassignites, from more or less hydrous, chlorine-rich parental magmas (Filiberto et al., 2016a, 2016b). In fact, the presence of Cl in a magma affects its liquidus as H_2O does, permitting the residual melt to evolve at lower temperatures before solidification (Filiberto and Treiman, 2009a, 2009b; Filiberto et al., 2014b; Farcy et al., 2016).

The veins and veinlets investigated in the present study are composed of a complex assemblage of phyllosilicates corresponding to the mineral assemblage described as “iddingsite” by early authors (Ross and Shannon, 1925; Edwards, 1938; Sun, 1957; Baker and Haggerty, 1967; Haggerty and Baker, 1967; Eggleton, 1984). In line with the present study, a number of previous studies concluded on the deuteric origin of iddingsite found in some terrestrial or Martian rocks, i.e. a

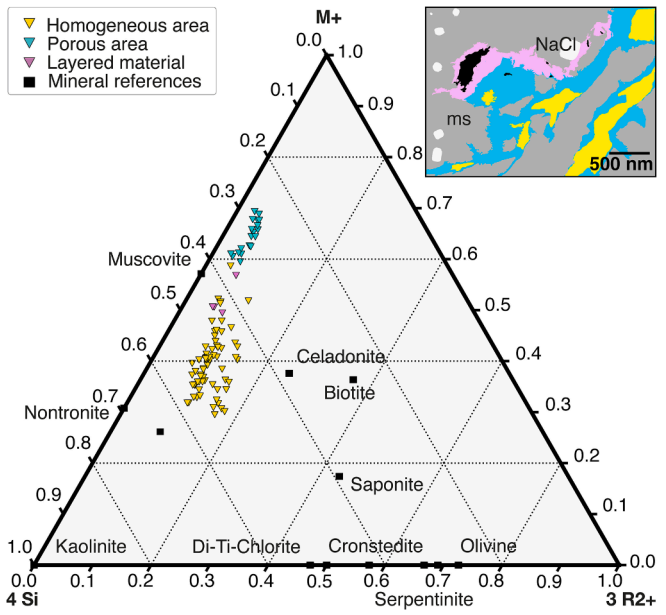

Fig. 10. Triplot ($M^{\pm}$-4Si-3R^{2+} ternary plot) showing the chemical compositions of the different parts of the mesostasis vein estimated from EDXS data. The $M^{\pm}$ pole represents the total electrical charge provided by interlayer cations (Na + K + 2Ca), the 4Si pole represents the tetrahedral charge (Si/4), and the 3R pole represents the number of bivalent ions integrated in the octahedral sheets with 3R = (Mg^{2+} + Fe^{2+} + Mn^{2+})/3. Note that the content in Fe^{2+} has been considered as being close to zero given the resemblance between the XANES spectra of these phyllosilicates with that of the 100 % Fe^{3+} reference from Bourdelle et al. (2013). The schematics diagram on the right shows the distribution of the different phases with the same color code.

precipitation from a magmatic fluid altering pre-existing silicates. For instance, Andreani et al. (2023) recently reported the occurrence of fluid-rich iddingsite-like inclusions in olivines from troctolites exhumed along the Mid-Atlantic Ridge. The isotopic composition of these inclusions indicates that the fluid was produced during magma degassing. Earlier, Clément et al. (2007) reported olivine crystals hosting "high temperature iddingsite" (HTI) rich in Fe^{3+} (Fe^{3+}/Fe = 80 %) in gabbros from Maupiti (French Polynesia). As the micaceous-celadonite internal part of the veins in NWA 817 *(*Fig. 4 *and* Table 1*)*, the central part of the Maupiti HTI exhibits higher Ca, Al, Mg and Fe contents and a lower Si content than the adjacent porous external part and its hosting olivine. The authors concluded that the Maupiti HTI results from modifications of the structure of olivine due to intense hydroxylation and Fe-oxidation taking place at high temperatures, likely between 600–1000 °C. Another recent study relying on mineralogical investigations of Precambrian monzogabbros from Kansas (USA) concluded on the magmatic origin of veins intersecting olivines (Combaudon et al., 2024). Identified as iddingsite, these veins exhibit a structuration with internal and external parts and are composed of micas associated with serpentines and chlorites interpreted as products of deuteric alteration. Consistently, Kuebler (2013) and Kizovski et al. (2020) interpreted iddingsite veins intersecting olivines in Martian shergottites (ALH 77005, NWA 10416 and NWA 7042) as products of deuteric alteration having occurred at high temperature, during magma cooling, before the total solidification of the rock. Rather than evidencing the past circulation of liquid water at the surface of the red planet, the occurrence of these phases in shergottites rather suggests the existence of a relatively water-rich magmatic reservoir on Mars (Kuebler, 2013; Kizovski et al., 2020). All these reports strengthen the present interpretation of iddingsite in NWA 817 as the product of the oxidative deuteric alteration of olivine.

4.3. Discrepancies with previous studies

Most of previous studies have interpreted iddingsite-like assemblages in Nakhlites as secondary assemblages produced during the late alteration of the hosting mesostasis by secondary circulating fluids after the entire consolidation of the rocks (e.g., Bridges and Schwenzer, 2012). In Lafayette, Nakhla and Governador Valadares, this interpretation is supported by the association of iddingsite-like assemblages with evaporite minerals, such as siderite, gypsum, and anhydrite (Gooding et al., 1991; Bridges and Grady, 2000; Changela and Bridges, 2010; Bridges and Schwenzer, 2012; Hicks et al., 2014; Piercy et al., 2022). A common explanation for the occurrence of these mineral associations is the secondary circulation of CO_2-rich fluids which can result from either impact-generated hydrothermal circulation (Bridges and Grady, 2000; Changela and Bridges, 2010; Bridges and Schwenzer, 2012; Hicks et al., 2014; Piercy et al., 2022) or percolation of CO_2-rich meteoritic water (Tomkinson et al., 2013; Lee et al., 2015). For instance, Hicks et al. (2014) interpreted the production of iddingsite veins in Lafayette as the result of the circulation of a CO_2-rich hydrothermal fluid (~150–200 °C), likely created by an impact-induced melting of subsurface ice (a scenario later adopted by (Piercy et al., 2022). In contrast, Tomkinson et al. (2013) proposed a detailed scenario for the formation of iddingsite veins in Lafayette, involving the centripetal replacement of olivine as a result from the circulation of a meteoritic CO_2-rich fluid in equilibrium with the atmosphere (a scenario later adopted by Lee et al., 2015). As per these scenarii, the alteration of olivine led to the production of a ferrous saponite vein which was then replaced by siderite, in turn replaced in the central part of the vein by Fe-rich smectite.

Yet, in contrast to Lafayette, NWA 817 does not contain Martian carbonates (Hicks et al., 2014). Plus, the mesostasis of NWA 817 does not show any evidence of alteration, which, if it had occurred, would have produced Al-rich secondary minerals, like zeolites for instance (Meunier and Velde, 2004). Also, the olivine-hosted veins in NWA 817 are not equivalent to the veins reported in Lafayette (Hicks et al., 2014). Precisely, the ferric saponite in Lafayette exhibits a high Mg content (18.6 at.%) and a rather low Fe content (9 at.% of Fe^{2+}, 12 at.% of Fe^{3+}VI, 3 at.% of Fe^{3+}IV) (Hicks et al., 2014), which is not the case of the smectites composing the external part of the veins in NWA 817 (7.5 at.% of Mg, 40 at.% of Fe). Plus, the SAED patterns of the Fe-rich smectites in NWA 817 exhibit a 06.33 reflection at 1.55 Å and a 0.211 reflection at 4.52, which is consistent with FeIII nontronite (Baron et al., 2016; Fox et al., 2021). Last, neither the secondary alteration of feldspars or smectites produces micas (Wilson, 1999). In fact, in contrast to phases typical of secondary aqueous alteration, the occurrence of micas in the veins of NWA 817 rather points to a high temperature (i.e. magma-driven) crystallization rather than to a low temperature process (i.e. secondary alteration).

Altogether, a single tardi-magmatic sequence, having occurred at the end of the cooling process, thus more adequately explains the origin of the iddingsite-like assemblages in NWA 817, unlike in other Nakhlites such as Lafayette for which the circulation of an exogenous, secondary fluid circulation is required to produce carbonates at some point. These differences among Nakhlites may be explained by their respective positions within the various flows from which the Nakhlites originate. Distinct lava flows or lobes may have experienced different secondary fluid circulations. Plus, according to the proposed spatial organization of the different Nakhlites (Balta et al., 2017; Jambon et al., 2016; Udry and Day, 2018), Lafayette, Nakhla, and Governador Valdadores are positioned at the bottom of a distinct lava flow, while NWA 817 is described as having cooled at the top of another one, as is the case of Miller Range Nakhlites. The Nakhlites having crystallized at the bottom of lava flows likely underwent less decompression-induced cracking during extrusion, which likely limited the formation of magmatic iddingsite veins, as in Nakhla, Lafayette, and Governador Valdadores. In contrast, we anticipate that magmatic iddingsite veins similar to those reported here in NWA 817 may exist in other Nakhlites having cooled at the top of lava

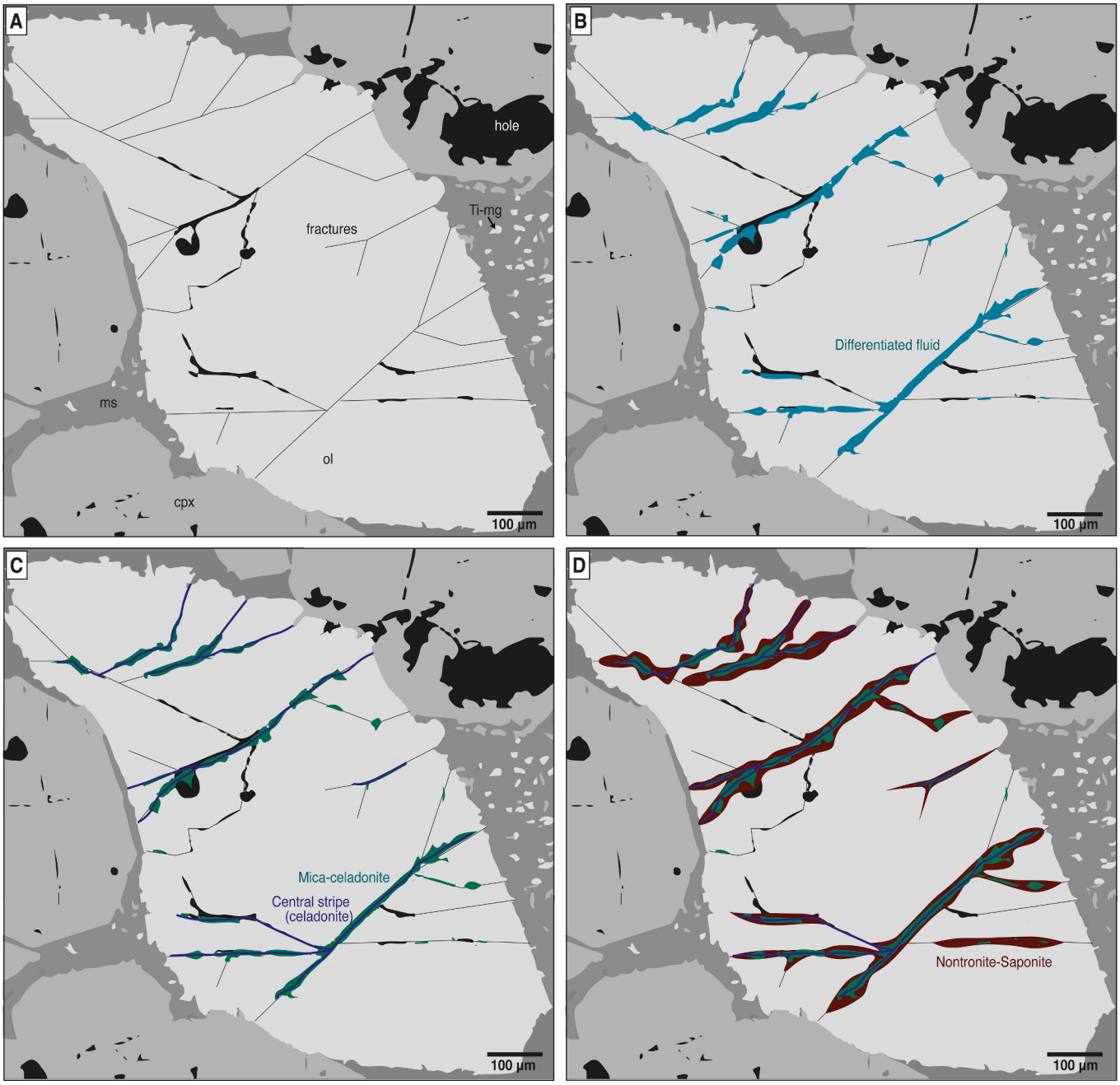

Fig. 11. Schematical illustration of the proposed scenario for the formation of the « iddingsite » veins in NWA 817. **(A)** Decompression induces the formation of fractures and cracks in the olivine. **(B)** A residual differentiated magmatic fluid with a micaceous composition originating from the mesostasis seeps into the olivine cracks, destabilizing the olivine and forming scalloped patterns at its contact. **(C)** The ferric mica-celadonite and the Mg-rich celadonite concomitantly precipitate, producing the internal part of the vein and the central stripe. **(B-4)** The residual fluid trapped in the fractures continues to dissolve the hosting olivine, producing the nontronite-saponite in the external part of the vein.

flows, such as the Miller Range Nakhlites (McCubbin et al., 2009; Hallis and Taylor, 2011; Martell et al., 2022).

5. Implications for the story of the Martian water

There is widespread evidence for water flowing on the surface of Mars (Carr, 1996; Squyres et al., 2004; Grotzinger et al., 2014; Kite and Conway, 2024). However, while there is clear evidence for ancient times, things are not that clear for the Amazonian period. With an age of 1340 ± 40 Myr (Bunch and Reid, 1975; Nyquist et al., 2001; Treiman, 2005; Udry and Day, 2018), Nakhlites and Chassignites are the only specimens of the Martian mid-Amazonian period available on Earth (Shergottites, sourced from the youngest volcanoes on Mars, are at least 600 Myr younger than Nakhlites and Chassignites – Jones, 2015; Cohen et al., 2023). According to the Rb-Sr and K-Ar datation of secondary smectites and carbonates, some Nakhlites such as Lafayette experienced aqueous alteration at the surface of Mars ~ 630 to 740 Myr ago (Borg and Drake, 2005; Tremblay et al., 2024), although Swindle et al. (2000) noted earlier that these ages may correspond to the secondary alteration of iddingsite rather than to its formation.

Here we show that iddingsite in some Nakhlites may not be a product of secondary aqueous alteration. In fact, we interpret the iddingsite-like assemblages occurring in NWA 817 as veins within olivines and as patches and veinlets within the mesostasis as tardi-magmatic, i.e. as

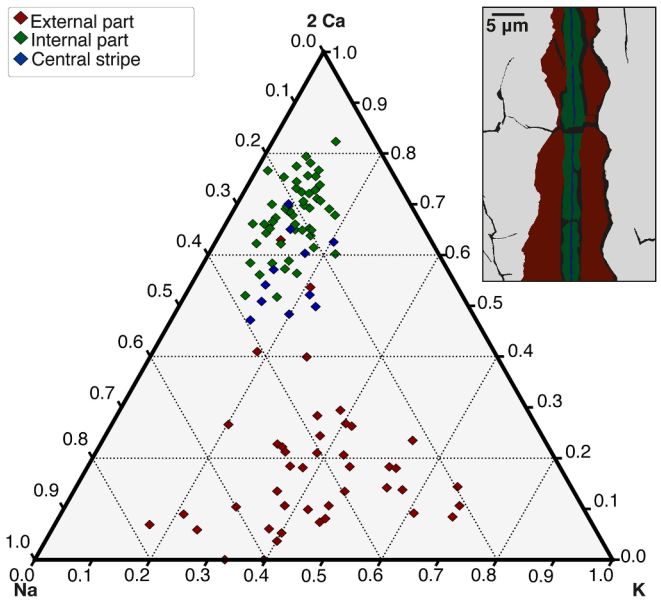

Fig. 12. Triplot (2Ca-Na-K ternary plot) showing the chemical compositions of the different parts of the olivine-hosted vein estimated from EDXS data. Such representation provides information on the nature of the cations within the interlayers of phyllosilicates. The schematics diagram on the right shows the most common tripartite organization of an olivine-hosted vein, with the external part of the vein, the internal part of the vein and the central stripe with the same color code.

phases having precipitated directly from a residual magmatic fluid and/or as a result of its interactions with olivines (i.e. oxidative deuteric alteration) during magma cooling (i.e. concomitantly with the solidification of the mesostasis). The mesostasis assemblages display poorly crystallized phases associated with well-crystallized phyllosilicates arranged around porous regions, resembling the tardi-magmatic clays described in Nakhla and NWA 5790 (Viennet et al., 2020, 2021). Olivine-hosted veins are symmetrically structured around the vein axis, with an internal part exhibiting a mica-celadonite composition and an external part displaying a nontronite-saponite composition. All these features are consistent with a progressive differentiation of a residual magmatic fluid having infiltrated the decompression-induced cracks of olivines at the end of the cooling sequence and initiated the oxidative deuteric dissolution of the hosting olivine, producing the ferric mica-celadonite phyllosilicates and, ultimately, the Fe-nontronite-saponite minerals.

Altogether, without excluding the possibility that other Nakhlites have experienced secondary alteration by surface water at some point of their history, either induced by impact-generated hydrothermal activity or weathering, the observations reported in the present study of NWA 817 rather suggest a tardi-magmatic production of iddingsite. Such magmatic production of clay minerals in a Martian meteorite archetypal of the Martian crust portends that a possibly significant fraction of the Fe/Mg clay minerals detected on Mars from orbit may not be the products of the aqueous alteration of preexisting silicates by (sub)surface water. The present study thus justifies a re-evaluation of the exact origin of the clay minerals detected on Mars so far, with potential consequences for our vision of both the magmatic and climatic histories of Mars.

CRediT authorship contribution statement

V. Megevand: Writing – original draft, Methodology, Investigation, Data curation, Conceptualization. **J.-C. Viennet:** Writing – original draft, Supervision, Methodology, Investigation, Data curation, Conceptualization. **C. Le Guillou:** Methodology, Investigation, Data curation. **F. Guyot:** Methodology, Investigation, Data curation. **S. Bernard:** Writing – original draft, Supervision, Project administration, Methodology, Investigation, Data curation, Conceptualization.

Data availability

All data used in the present study are publicly available at Zenodo with a Creative Commons Attribution 4.0 license at https://doi.org/10.5281/zenodo.14389473 (Megevand, 2024).

Declaration of competing interest

The authors declare that they have no known competing financial interests or personal relationships that could have appeared to influence the work reported in this paper.

Acknowledgments

The authors wish to acknowledge David Troadec (IEMN) for the extraction of FIB foils. Special thanks also go to Sylvain Pont for his expert support with the SEM, and Stefan Stanescu and Sufal Swaraj for their expert support with the HERMES STXM beamline at SOLEIL. The SEM facility is supported by the MNHN Plateforme de Microscopie Electronique. The TEM facility at the CCM (Lille University) is supported by the Chevreul Institute, the European FEDER and Region Nord-Pas-de-Calais. The HERMES beamline (SOLEIL) is supported by the CNRS, the CEA, the Region Ile de France, the Departmental Council of Essonne and the Region Centre.

References

Andreani, M., Montagnac, G., Fellah, C., Hao, J., Vandier, F., Daniel, I., Pisapia, C., Galipaud, J., Lilley, M.D., Früh Green, G.L., Borensztajn, S., Ménez, B., 2023. The rocky road to organics needs drying. *Nat. Commun.* 14, 347.

Baker, I., Haggerty, S.E., 1967. The alteration of olivine in basaltic and associated lavas: Part II: Intermediate and low temperature alteration. *Contrib. Mineral. Petrol.* 16, 258–273.

Balta, B.J., Sanborn, M.E., Mayne, R.G., Wadhwa, M., McSween, H.Y., Crossley, S.D., 2017. Northwest Africa 5790: a previously unsampled portion of the upper part of the nakhlite pile. Meteorit. Planet. Sci. 52, 36–59.

Baron, F., Petit, S., Tertre, E., Decarreau, A., 2016. Influence of aqueous Si and Fe speciation on tetrahedral Fe(III) substitutions in nontronites: a clay synthesis approach. *Clays Clay Miner.* 64, 230–244.

Belkhou, R., Stanescu, S., Swaraj, S., Besson, A., Ledoux, M., Hajlaoui, M., Dalle, D., 2015. HERMES: a soft X-ray beamline dedicated to X-ray microscopy. *J. Synchrotron Radiat.* 22, 968–979.

Berger, G., Meunier, A., Beaufort, D., 2014. Clay mineral formation on Mars: Chemical constraints and possible contribution of basalt out-gassing. *Planet. Space Sci.* 95, 25–32.

Berger, G., Beaufort, D., Antoine, R., 2018. Clay minerals related to the late magmatic activity of the Piton des Neiges (Réunion Island): consequence for the primitive crusts. *Clay Miner.* 53, 675–690.

Bernard, S., Benzerara, K., Beyssac, O., Brown, G.E., Stamm, L.G., Duringer, P., 2009. Ultrastructural and chemical study of modern and fossil sporoderms by Scanning Transmission X-ray Microscopy (STXM). *Rev. Palaeobot. Palynol.* 156, 248–261.

Borg, L., Drake, M.J., 2005. A review of meteorite evidence for the timing of magmatism and of surface or near-surface liquid water on Mars. J. Geophys. Res. Planets 110.

Bourdelle, F., Benzerara, K., Beyssac, O., Cosmidis, J., Neuville, D.R., Brown, G.E., Paineau, E., 2013. Quantification of the ferric/ferrous iron ratio in silicates by scanning transmission X-ray microscopy at the Fe L2,3 edges. *Contrib. Mineral. Petrol.* 166, 423–434.

Brett, R.C., Russell, J.K., Andrews, G.D.M., Jones, T.J., 2015. The ascent of kimberlite: Insights from olivine. *Earth Planet. Sci. Lett.* 424, 119–131.

Bridges, J., Grady, M., 2000. Evaporite mineral assemblages in the nakhlite (martian) meteorites. *Earth Planet. Sci. Lett.* 176, 267–279.

Bridges, J.C., Schwenzer, S.P., 2012. The nakhlite hydrothermal brine on Mars. *Earth Planet. Sci. Lett.* 359–360, 117–123.

Bristow, T.F., Rampe, E.B., Achilles, C.N., Blake, D.F., Chipera, S.J., Craig, P., Crisp, J.A., Des Marais, D.J., Downs, R.T., Gellert, R., 2018. Clay mineral diversity and abundance in sedimentary rocks of Gale crater. Mars. *Sci. Adv.* 4, eaar3330.

Bunch, T., Reid, A.M., 1975. The nakhlites Part I: Petrography and mineral chemistry. *Meteoritics* 10, 303–315.

Carr, M.H., 1996. *Water on mars*. Oxford University Press.

Carter, J., Poulet, F., Bibring, J.-P., Mangold, N., Murchie, S., 2013. Hydrous minerals on Mars as seen by the CRISM and OMEGA imaging spectrometers: Updated global view: HYDROUS MINERALS ON MARS: GLOBAL VIEW. *J. Geophys. Res. Planets* 118, 831–858.

Changela, H.G., Bridges, J.C., 2010. Alteration assemblages in the nakhlites: variation with depth on Mars: Alteration assemblages in the nakhlites. *Meteorit. Planet. Sci.* 45, 1847–1867.

Chevrier, V., Lorand, J., Sautter, V., 2011. Sulfide petrology of four nakhlites: Northwest Africa 817, Northwest Africa 998, Nakhla, and Governador Valadares. *Meteorit. Planet. Sci.* 46, 769–784.

Clément, J.-P., Caroff, M., Dudoignon, P., Launeau, P., Bohn, M., Cotten, J., Blais, S., Guille, G., 2007. A possible link between gabbros bearing High Temperature Iddingsite alteration and huge pegmatoid intrusions: The Society Islands, French Polynesia. *Lithos* 96, 524–542.

Cohen, B.E., Mark, D.F., Cassata, W.S., Kalnins, L.M., Lee, M.R., Smith, C.L., Shuster, D. L., 2023. Synchronising rock clocks of Mars' history: Resolving the shergottite 40Ar/39Ar age paradox. *Earth Planet. Sci. Lett.* 621, 118373.

Combaudon, V., Sissmann, O., Bernard, S., Viennet, J.-C., Megevand, V., Le Guillou, C., Guélard, J., Martinez, I., Guyot, F., Derluyn, H., Deville, E., 2024. Are the Fe-rich-clay veins in the igneous rock of the Kansas (USA) Precambrian crust of magmatic origin? *Lithos* 474–475, 107583.

de la Peña, F., Ostasevicius, T., Fauske, V.T., Burdet, P., Jokubauskas, P., Nord, M., Sarahan, M., Prestat, E., Johnstone, D.N., Taillon, J., 2017. Electron microscopy (big and small) data analysis with the open source software package HyperSpy. *Microsc. Microanal.* 23, 214–215.

DePasquale, B.M., Jenkins, D.M., 2022. The upper-thermal stability of an iron-rich smectite: Implications for smectite formation on Mars. *Icarus* 374, 114816.

Ding, Z., Frost, R.L., 2002. Controlled rate thermal analysis of nontronite. *Thermochim. Acta* 389, 185–193.

Edwards, A., 1938. The formation of iddingsite. *Am. Mineral. J. Earth Planet. Mater.* 23, 277–281.

Eggleton, R.A., 1984. Formation of iddingsite rims on olivine: a transmission electron microscope study. *Clays Clay Miner.* 32, 1–11.

Evans, B.W., Kuehner, S.M., Joswiak, D.J., Cressey, G., 2017. Serpentine, Iron-rich Phyllosilicates and Fayalite Produced by Hydration and Mg Depletion of Peridotite, Duluth Complex, Minnesota, USA. *J. Petrol.* 58, 495–512.

Evans, O., Spiegelman, M., Kelemen, P.B., 2020. Phase-field modeling of reaction-driven cracking: determining conditions for extensive olivine serpentinization. *J. Geophys. Res. Solid Earth* 125, e2019JB018614.

Farcy, B.J., Gross, J., Carpenter, P., Hicks, J., Filiberto, J., 2016. Effect of chlorine on near-liquidus crystallization of olivine-phyric shergottite NWA 6234 at 1 GP a: implication for volatile-induced melting of the Martian mantle. *Meteorit. Planet. Sci.* 51, 2011–2022.

Filiberto, J., Dasgupta, R., Gross, J., Treiman, A.H., 2014a. Effect of chlorine on near-liquidus phase equilibria of an Fe–Mg-rich tholeiitic basalt. *Contrib. Mineral. Petrol.* 168, 1027.

Filiberto, J., Baratoux, D., Beaty, D., Breuer, D., Farcy, B.J., Grott, M., Jones, J.H., Kiefer, W.S., Mane, P., McCubbin, F.M., Schwenzer, S.P., 2016a. A review of volatiles in the Martian interior. *Meteorit. Planet. Sci.* 51, 1935–1958.

Filiberto, J., Gross, J., McCubbin, F.M., 2016b. Constraints on the water, chlorine, and fluorine content of the Martian mantle. *Meteorit. Planet. Sci.* 51, 2023–2035.

Filiberto, J., Treiman, A.H., 2009a. Martian magmas contained abundant chlorine, but little water. *Geology* 37, 1087–1090.

Filiberto, J., Treiman, A.H., 2009b. The effect of chlorine on the liquidus of basalt: first results and implications for basalt genesis on Mars and Earth. *Chem. Geol.* 263, 60–68.

Filiberto, J., Treiman, A.H., Giesting, P.A., Goodrich, C.A., Gross, J., 2014b. High-temperature chlorine-rich fluid in the martian crust: a precursor to habitability. *Earth Planet. Sci. Lett.* 401, 110–115.

Fox, V.K., Kupper, R.J., Ehlmann, B.L., Catalano, J.G., Razzell-Hollis, J., Abbey, W.J., Schild, D.J., Nickerson, R.D., Peters, J.C., Katz, S.M., White, A.C., 2021. Synthesis and characterization of Fe(III)-Fe(II)-Mg-Al smectite solid solutions and implications for planetary science. *Am. Mineral.* 106, 964–982.

Gillet, Ph., Barrat, J.A., Deloule, E., Wadhwa, M., Jambon, A., Sautter, V., Devouard, B., Neuville, D., Benzerara, K., Lesourd, M., 2002. Aqueous alteration in the Northwest Africa 817 (NWA 817) Martian meteorite. *Earth Planet. Sci. Lett.* 203, 431–444.

Goff, F., 1996. Vesicle cylinders in vapor-differentiated basalt flows. *J. Volcanol. Geotherm. Res.* 71, 167–185.

Gooding, J.L., Wentworth, S.J., Zolensky, M.E., 1991. Aqueous alteration of the Nakhla meteorite. *Meteoritics* 26, 135–143.

Grauby, O., Petit, S., Decarreau, A., Baronnet, A., 1994. The nontronite-saponite series: an experimental approach. *Eur. J. Mineral.* 99–112.

Grigor'ev, D.P., Brenner, Y., 1965. Ontogeny of minerals. *No Title*.

Grotzinger J. P., Sumner D. Y., Kah L. C., Stack K., Gupta S., Edgar L., Rubin D., Lewis K., Schieber J., Mangold N., Milliken R., Conrad P. G., DesMarais D., Farmer J., Siebach K., Calef F., Hurowitz J., McLennan S. M., Ming D., Vaniman D., Crisp J., Vasavada A., Edgett K. S., Malin M., Blake D., Gellert R., Mahaffy P., Wiens R. C., Maurice S., Grant J. A., Wilson S., Anderson R. C., Beegle L., Arvidson R., Hallet B., Sletten R. S., Rice M., Bell J., Griffes J., Ehlmann B., Anderson R. B., Bristow T. F., Dietrich W. E., Dromart G., Eigenbrode J., Fraeman A., Hardgrove C., Herkenhoff K., Jandura L., Kocurek G., Lee S., Leshin L. A., Leveille R., Limonadi D., Maki J., McCloskey S., Meyer M., Minitti M., Newsom H., Oehler D., Okon A., Palucis M., Parker T., Rowland S., Schmidt M., Squyres S., Steele A., Stolper E., Summons R., Treiman A., Williams R., Yingst A., Team M. S., Kemppinen O., Bridges N., Johnson J. R., Cremers D., Godber A., Wadhwa M., Wellington D., McEwan I., Newman C., Richardson M., Charpentier A., Peret L., King P., Blank J., Weigle G., Li S., Robertson K., Sun V., Baker M., Edwards C., Farley K., Miller H., Newcombe M., Pilorget C., Brunet C., Hipkin V., Leveille R., Marchand G., Sanchez P. S., Favot L., Cody G., Fluckiger L., Lees D., Nefian A., Martin M., Gailhanou M., Westall F., Israel G., Agard C., Baroukh J., Donny C., Gaboriaud A., Guillemot P., Lafaille V., Lorigny E., Paillet A., Perez R., Saccoccio M., Yana C., Armiens-Aparicio C., Rodriguez J. C., Blazquez I. C., Gomez F. G., Gomez-Elvira J., Hettrich S., Malvitte A. L., Jimenez M. M., Martinez-Frias J., Martin-Soler J., Martin-Torres F. J., Jurado A. M., Mora-Sotomayor L., Caro G. M., Lopez S. N., Peinado-Gonzalez V., Pla-Garcia J., Manfredi J. A. R., Romeral-Planello J. J., Fuentes S. A. S., Martinez E. S., Redondo J. T., Urqui-O'Callaghan R., Mier M.-P. Z., Chipera S., Lacour J.-L., Mauchien P., Sirven J.-B., Manning H., Fairen A., Hayes A., Joseph J., Sullivan R., Thomas P., Dupont A., Lundberg A., Melikechi N., Mezzacappa A., DeMarines J., Grinspoon D., Reitz G., Prats B., Atlaskin E., Genzer M., Harri A.-M., Haukka H., Kahanpaa H., Kauhanen J., Paton M., Polkko J., Schmidt W., Siili T., Fabre C., Wray J., Wilhelm M. B., Poitrasson F., Patel K., Gorevan S., Indyk S., Paulsen G., Bish D., Gondet B., Langevin Y., Geffroy C., Baratoux D., Berger G., Cros A., d'Uston C., Forni O., Gasnault O., Lasue J., Lee Q.-M., Meslin P.-Y., Pallier E., Parot Y., Pinet P., Schroder S., Toplis M., Lewin E., Brunner W., Heydari E., Achilles C., Sutter B., Cabane M., Coscia D., Szopa C., Robert F., Sautter V., Le Mouelic S., Nachon M., Buch A., Stalport F., Coll P., Francois P., Raulin F., Teinturier S., Cameron J., Clegg S., Cousin A., DeLapp D., Dingler R., Jackson R. S., Johnstone S., Lanza N., Little C., Nelson T., Williams R. B., Jones A., Kirkland L., Baker B., Cantor B., Caplinger M., Davis S., Duston B., Fay D., Harker D., Herrera P., Jensen E., Kennedy M. R., Krezoski G., Krysak D., Lipkaman L., McCartney E., McNair S., Nixon B., Posiolova L., Ravine M., Salamon A., Saper L., Stoiber K., Supulver K., Van Beek J., Van Beek T., Zimdar R., French K. L., Iagnemma K., Miller K., Goesmann F., Goetz W., Hviid S., Johnson M., Lefavor M., Lyness E., Breves E., Dyar M. D., Fassett C., Edwards L., Haberle R., Hoehler T., Hollingsworth J., Kahre M., Keely L., McKay C., Bleacher L., Brinckerhoff W., Choi D., Dworkin J. P., Floyd M., Freissinet C., Garvin J., Glavin D., Harpold D., Martin D. K., McAdam A., Pavlov A., Raaen E., Smith M. D., Stern J., Tan F., Trainer M., Posner A., Voytek M., Aubrey A., Behar A., Blaney D., Brinza D., Christensen L., DeFlores L., Feldman J., Feldman S., Flesch G., Jun I., Keymeulen D., Mischna M., Morookian J. M., Pavri B., Schoppers M., Sengstacken A., Simmonds J. J., Spanovich N., Juarez M. d. l. T., Webster C. R., Yen A., Archer P. D., Cucinotta F., Jones J. H., Morris R. V., Niles P., Rampe E., Nolan T., Fisk M., Radziemski L., Barraclough B., Bender S., Berman D., Dobrea E. N., Tokar R., Cleghorn T., Huntress W., Manhes G., Hudgins J., Olson T., Stewart N., Sarrazin P., Vicenzi E., Bullock M., Ehresmann B., Hamilton V., Hassler D., Peterson J., Rafkin S., Zeitlin C., Fedosov F., Golovin D., Karpushkina N., Kozyrev A., Litvak M., Malakhov A., Mitrofanov I., Mokrousov M., Nikiforov S., Prokhorov V., Sanin A., Tretyakov V., Varenikov A., Vostrukhin A., Kuzmin R., Clark B., Wolff M., Botta O., Drake D., Bean K., Lemmon M., Schwenzer S. P., Lee E. M., Sucharski R., Hernandez M. A. d. P., Avalos J. J. B., Ramos M., Kim M.-H., Malespin C., Plante I., Muller J.-P., Navarro-Gonzalez R., Ewing R., Boynton W., Downs R., Fitzgibbon M., Harshman K., Morrison S., Kortmann O., Williams A., Lugmair G., Wilson M. A., Jakosky B., Balic-Zunic T., Frydenvang J., Jensen J. K., Kinch K., Koefoed A., Madsen M. B., Stipp S. L. S., Boyd N., Campbell J. L., Perrett G., Pradler I., VanBommel S., Jacob S., Owen T., Savijarvi H., Boehm E., Bottcher S., Burmeister S., Guo J., Kohler J., Garcia C. M., Mueller-Mellin R., Wimmer-Schweingruber R., Bridges J. C., McConnochie T., Benna M., Franz H., Bower H., Brunner A., Blau H., Boucher T., Carmosino M., Atreya S., Elliott H., Halleaux D., Renno N., Wong M., Pepin R., Elliott B., Spray J., Thompson L., Gordon S., Ollila A., Williams J., Vasconcelos P., Bentz J., Nealson K., Popa R., Moersch J., Tate C., Day M., Francis R., McCullough E., Cloutis E., ten Kate I. L., Scholes D., Slavney S., Stein T., Ward J., Berger J., Moores, J.E., 2014. A Habitable Fluvio-Lacustrine Environment at Yellowknife Bay, Gale Crater, Mars. Science 343, 1242777–1242777.

Haggerty, S.E., Baker, I., 1967. The alteration of olivine in basaltic and associated lavas: Part I: high temperature alteration. *Contrib. Mineral. Petrol.* 16, 233–257.

Hallis, L.J., Taylor, G.J., 2011. Comparisons of the four Miller Range nakhlites, MIL 03346, 090030, 090032 and 090136: Textural and compositional observations of primary and secondary mineral assemblages. *Meteorit. Planet. Sci.* 46, 1787–1803.

Hayman, P.C., Cas, R.A.F., Johnson, M., 2008. Difficulties in distinguishing coherent from fragmental kimberlite: A case study of the Muskox pipe (Northern Slave Province, Nunavut, Canada). *J. Volcanol. Geotherm. Res.* 174, 139–151.

Hicks, L.J., Bridges, J.C., Gurman, S.J., 2014. Ferric saponite and serpentine in the nakhlite martian meteorites. *Geochim. Cosmochim. Acta* 136, 194–210.

Jambon, A., Sautter, V., Barrat, J.-A., Gattacceca, J., Rochette, P., Boudouma, O., Badia, D., Devouard, B., 2016. Northwest Africa 5790: Revisiting nakhlite petrogenesis. *Geochim. Cosmochim. Acta* 190, 191–212.

Jones, J.H., 2015. Various aspects of the petrogenesis of the Martian shergottite meteorites. *Meteorit. Planet. Sci.* 50, 674–690.

Kalo, H., Möller, M.W., Ziadeh, M., Dolejš, D., Breu, J., 2010. Large scale melt synthesis in an open crucible of Na-fluorohectorite with superb charge homogeneity and particle size. *Appl. Clay Sci.* 48, 39–45.

Kelley, D.S., 1996. Methane-rich fluids in the oceanic crust. *J. Geophys. Res. Solid Earth* 101, 2943–2962.

Kite, E.S., Conway, S., 2024. Geological evidence for multiple climate transitions on Early Mars. *Nat. Geosci.* 1–10.

Kizovski, T.V., Izawa, M.R.M., Tait, K.T., Moser, D.E., Day, J.M.D., Hyde, B.C., White, L. F., Kovarik, L., Taylor, S.D., Perea, D.E., Barker, I.R., Joy, B.R., 2020. Petrogenesis, alteration, and shock history of intermediate shergottite Northwest Africa 7042: Evidence for hydrous magmatism on Mars? *Geochim. Cosmochim. Acta* 283, 103–123.

Kloprogge, J.T., Ponce, C.P., 2021. Spectroscopic studies of synthetic and natural saponites: a review. *Minerals* 11, 112.

Krämer, R.L., Gattacceca, J., Devouard, B., Udry, A., Debaille, V., Rochette, P., Lorand, J.-P., Bonal, L., Beck, P., Sautter, V., Busemann, H., Meier, M.M.M., Maden, C., Hublet, G., Martinez, R., 2020. Caleta el Cobre 022 Martian meteorite: Increasing nakhlite diversity. *Meteorit. Planet. Sci.* 55, 1539–1563.

Krämer Ruggiu, L., Devouard, B., Gattacceca, J., Bonal, L., Piani, L., Leroux, H., Grauby, O., 2024. Multistaage aqueous alteration in CeC 022 and other nakhlites. Meteorit. Planet. Sci.

Kuebler, K.E., 2013. A comparison of the iddingsite alteration products in two terrestrial basalts and the Allan Hills 77005 martian meteorite using Raman spectroscopy and electron microprobe analyses: comparison of iddingsite alteration products. *J. Geophys. Res. Planets* 118, 803–830.

Le Guillou, C., Brearley, A., 2014. Relationships between organics, water and early stages of aqueous alteration in the pristine CR3.0 chondrite MET 00426. *Geochim. Cosmochim. Acta* 131, 344–367.

Le Guillou, C., Changela, H.G., Brearley, A.J., 2015. Widespread oxidized and hydrated amorphous silicates in CR chondrites matrices: Implications for alteration conditions and H2 degassing of asteroids. *Earth Planet. Sci. Lett.* 420, 162–173.

Le Guillou, C., Zanetta, P.M., Leroux, H., Blanchenet, A.M., Marinova, M., 2024. Light Element (C, N, O) Quantification by EDXS: Application to Meteorite Water Content and Organic Composition. Microsc. Microanal. 30 (4), 660–670.

Lee, M.R., Chatzitheodoridis, E., 2016. Replacement of glass in the Nakhla meteorite by berthierine: Implications for understanding the origins of aluminum-rich phyllosilicates on Mars. *Meteorit. Planet. Sci.* 51, 1643–1653.

Lee, M.R., Tomkinson, T., Hallis, L.J., Mark, D.F., 2015. Formation of iddingsite veins in the martian crust by centripetal replacement of olivine: Evidence from the nakhlite meteorite Lafayette. *Geochim. Cosmochim. Acta* 154, 49–65.

Lee, M.R., Daly, L., Cohen, B.E., Hallis, L.J., Griffin, S., Trimby, P., Boyce, A., Mark, D.F., 2018. Aqueous alteration of the Martian meteorite Northwest Africa 817: Probing fluid-rock interaction at the nakhlite launch site. *Meteorit. Planet. Sci.* 53, 2395–2412.

Martell, J., Alwmark, C., Daly, L., Hall, S., Alwmark, S., Woracek, R., Hektor, J., Helfen, L., Tengattini, A., Lee, M., 2022. The scale of a martian hydrothermal system explored using combined neutron and x-ray tomography. *Sci. Adv.* 8, eabn3044.

McCubbin, F.M., Tosca, N.J., Smirnov, A., Nekvasil, H., Steele, A., Fries, M., Lindsley, D. H., 2009. Hydrothermal jarosite and hematite in a pyroxene-hosted melt inclusion in martian meteorite Miller Range (MIL) 03346: Implications for magmatic-hydrothermal fluids on Mars. *Geochim. Cosmochim. Acta* 73, 4907–4917.

Megevand, V., 2024. Data collected on NWA 817 by Megevand et al.

Meunier, A., 2005. *Clays*. Springer-Verlag, Berlin/Heidelberg.

Meunier, A., Mas, A., Beaufort, D., Patrier, P., Dudoignon, P., 2008. Clay minerals in basalt-hawaiite rocks from Mururoa Atoll (French Polynesia). II. Petrography and Geochemistry. *Clays Clay Miner.* 56, 730–750.

Meunier, A., Petit, S., Ehlmann, B.L., Dudoignon, P., Westall, F., Mas, A., El Albani, A., Ferrage, E., 2012. Magmatic precipitation as a possible origin of Noachian clays on Mars. *Nat. Geosci.* 5, 739–743.

Meunier, A., Velde, B., 2004. The Geology of Illite. In: *Illite* Springer. Berlin Heidelberg, Berlin, Heidelberg, pp. 63–143.

Meunier, A., Caner, L., Hubert, F., El Albani, A., Pret, D., 2013. The weathering intensity scale (WIS): An alternative approach of the Chemical Index of Alteration (CIA). *Am. J. Sci.* 313, 113–143.

Meunier, A., Velde, B., 1989. Solid solutions in I/S mixed-layer minerals and illite. *Am. Mineral.* 74, 1106–1112.

Mitchell, R.H., Skinner, E.M.W., Scott Smith, B.H., 2009. Tuffisitic kimberlites from the Wesselton Mine, South Africa: Mineralogical characteristics relevant to their formation. *Lithos* 112, 452–464.

Nakazawa, H., Yamada, H., Fujita, T., 1992. Crystal synthesis of smectite applying very high pressure and temperature. *Appl. Clay Sci.* 6, 395–401.

Noguchi, T., Nakamura, T., Misawa, K., Imae, N., Aoki, T., Toh, S., 2009. Laihunite and jarosite in the Yamato 00 nakhlites: Alteration products on Mars?: Laihunite and jarosite in nakhlites. *J. Geophys. Res. Planets* 114, n/a-n/a.

Nyquist, L.E., Bogard, D.D., Shih, C.Y., Greshake, A., Stöffler, D., Eugster, O., 2001. Ages and Geologic Histories of Martian Meteorites. *Space Sci. Rev.* 96, 105–164.

Piercy, J.D., Bridges, J.C., Hicks, L.J., 2022. Carbonate dissolution and replacement by odinite and saponite in the Lafayette nakhlite: Part of the CO2-CH4 cycle on Mars? *Geochim. Cosmochim. Acta* 326, 97–118.

Rampe, E.B., Blake, D.F., Bristow, T., Ming, D.W., Vaniman, D., Morris, R., Achilles, C., Chipera, S., Morrison, S., Tu, V., 2020. Mineralogy and geochemistry of sedimentary rocks and eolian sediments in Gale crater, Mars: A review after six Earth years of exploration with Curiosity. *Geochemistry* 80, 125605.

Ross, C.S., Shannon, E.V., 1925. The origin, occurrence, composition, and physical properties of the mineral iddingsite. *Proc. u. s. Natl. Mus.* 67, 1–19.

Saltas, V., Pentari, D., Vallianatos, F., 2020. Complex electrical conductivity of biotite and muscovite micas at elevated temperatures: a comparative study. *Materials* 13, 3513.

Sautter, V., Barrat, J.A., Jambon, A., Lorand, J.P., Gillet, P., Javoy, M., Joron, J.L., Lesourd, M., 2002. A new Martian meteorite from Morocco: the nakhlite North West Africa 817. *Earth Planet. Sci. Lett.* 195, 223–238.

Schenato, F., Formoso, M., Dudoignon, P., Meunier, A., Proust, D., Mas, A., 2003. Alteration processes of a thick basaltic lava flow of the Paraná Basin (Brazil): petrographic and mineralogical studies. *J. South Am. Earth Sci.* 16, 423–444.

Schiffbauer, J.D., Xiao, S., 2009. Novel application of focused ion beam electron microscopy (FIB-EM) in preparation and analysis of microfossil ultrastructures: a new view of complexity in early Eukaryotic organisms. *PALAIOS* 24, 616–626.

Simon, J., Hickman-Lewis, K., Cohen, B., Mayhew, L., Shuster, D., Debaille, V., Hausrath, E., Weiss, B., Bosak, T., Zorzano, M.-P., 2023. Samples collected from the floor of Jezero Crater with the Mars 2020 Perseverance Rover. *J. Geophys. Res. Planets* 128, e2022JE007474.

Squyres, S.W., Grotzinger, J.P., Arvidson, R.E., Bell III, J.F., Calvin, W., Christensen, P.R., Clark, B.C., Crisp, J., Farrand, W.H., Herkenhoff, K.E., 2004. In situ evidence for an ancient aqueous environment at Meridiani Planum. Mars. *Science* 306, 1709–1714.

Sun, M.-S., 1957. The nature of iddingsite in some basaltic rocks of New Mexico. Am. Mineral. J. Earth Planet. Mater. 42, 525–533.

Sun, V.Z., Milliken, R.E., 2015. Ancient and recent clay formation on Mars as revealed from a global survey of hydrous minerals in crater central peaks. *J. Geophys. Res. Planets* 120, 2293–2332.

Swaraj, S., Belkhou, R., Stanescu, S., Rioult, M., Besson, A., Hitchcock, A.P., 2017. Performance of the HERMES beamline at the carbon K-edge. *J. Phys. Conf. Ser.* 849, 012046.

Swindle, T.D., Treiman, A.H., Lindstrom, D.J., Burkland, M.K., Cohen, B.A., Grier, J.A., Li, B., Olson, E.K., 2000. Noble gases in iddingsite from the Lafayette meteorite: Evidence for liquid water on Mars in the last few hundred million years. *Meteorit. Planet. Sci.* 35, 107–115.

Tamura, K., Yamada, H., Nakazawa, H., 2000. Stepwise hydration of high-quality synthetic smectite with various cations. *Clays Clay Miner.* 48, 400–404.

Tomkinson, T., Lee, M.R., Mark, D.F., Smith, C.L., 2013. Sequestration of Martian CO2 by mineral carbonation. *Nat. Commun.* 4, 2662.

Treiman, A.H., 2005. The nakhlite meteorites: Augite-rich igneous rocks from Mars. *Geochemistry* 65, 203–270.

Treiman, A.H., Barrett, R.A., Gooding, J.L., 1993. Preterrestrial aqueous alteration of the Lafayette (SNC) meteorite. *Meteoritics* 28, 86–97.

Treiman, A.H., Gleason, J.D., Bogard, D.D., 2000. The SNC meteorites are from Mars. *Planet. Space Sci.* 48, 1213–1230.

Tremblay, M.M., Mark, D.F., Barfod, D.N., Cohen, B.E., Ickert, R.B., Lee, M.R., Tomkinson, T., Smith, C.L., 2024. Dating recent aqueous activity on Mars. *Geochem. Perspect. Lett.* 32, 58–62.

Udry, A., Day, J.M.D., 2018. 1.34 billion-year-old magmatism on Mars evaluated from the co-genetic nakhlite and chassignite meteorites. *Geochim. Cosmochim. Acta* 238, 292–315.

Udry, A., Howarth, G.H., Herd, C.D.K., Day, J.M.D., Lapen, T.J., Filiberto, J., 2020. What Martian Meteorites Reveal About the Interior and Surface of Mars. *J. Geophys. Res. Planets* 125, e2020JE006523.

Velbel, M.A., 2009. Dissolution of olivine during natural weathering. *Geochim. Cosmochim. Acta* 73, 6098–6113.

Viennet, J.-C., Bernard, S., Le Guillou, C., Sautter, V., Schmitt-Kopplin, P., Beyssac, O., Pont, S., Zanda, B., Hewins, R., Remusat, L., 2020. Tardi-magmatic precipitation of Martian Fe/Mg-rich clay minerals via igneous differentiation. *Geochem. Perspect. Lett.* 47–52.

Viennet, J.-C., Bernard, S., Le Guillou, C., Sautter, V., Grégoire, B., Jambon, A., Pont, S., Beyssac, O., Zanda, B., Hewins, R., Remusat, L., 2021. Martian Magmatic Clay Minerals Forming Vesicles: Perfect Niches for Emerging Life? *Astrobiology* 21, 605–612.

Wang, J., Morin, C., Li, L., Hitchcock, A.P., Scholl, A., Doran, A., 2009. Radiation damage in soft X-ray microscopy. *J. Electron Spectrosc. Relat. Phenom.* 170, 25–36.

Wilson, M.J., 1999. The origin and formation of clay minerals in soils: past, present and future perspectives. *Clay Miner.* 34, 7–25.

Wirth, R., 2009. Focused Ion Beam (FIB) combined with SEM and TEM: Advanced analytical tools for studies of chemical composition, microstructure and crystal structure in geomaterials on a nanometre scale. *Chem. Geol.* 261, 217–229.

Yamada, H., 1995. Cooling rate dependency of the formation of smectite crystals from a high-pressure and high-temperature hydrous melt. *Clays Clay Miner.* 43, 693–696.

Yamada, H., Nakazawa, H., Hashizume, H., 1994. Formation of smectite crystals at high pressures and temperatures. *Clays Clay Miner.* 42, 674–678.